Statistical Shape Modeling of Thoracic Aortic Aneurysms

A THESIS

SUBMITTED TO THE FACULTY OF THE

UNIVERSITY OF MINNESOTA

BY

Shion Matsumoto

IN PARTIAL FULFILLMENT OF THE REQUIREMENTS

FOR THE DEGREE OF

MASTER OF SCIENCE

Victor H. Barocas

May, 2021

Acknowledgements

I would like to thank my advisor Professor Victor Barocas for his support and guidance on this thesis and for the opportunity to explore my research interests. I would also like to thank my lab mates, colleagues, and friends for making my time in graduate school an enjoyable one. Special thanks to Haider, Jonathan, Louis, Stephan, and Stephanie. Lastly, I would like to thank my family for their unwavering support in my studies.

Abstract

The current framework for the statistical shape modeling of the aorta involves the parameterization of a mesh of the thoracic aorta onto a periodic rectangular parametric domain defined by the longitudinal and circumferential axes. Through parameterization onto a common parametric domain, dimension reduction techniques such as principal component analysis can be used to study the morphological characteristics of the vessels. The parameterization, however, requires that the mesh be homeomorphic to a cylinder; thus branching vessels cannot be included in the original geometry. This thesis presents a new feature that can be included in addition to the coordinates of each vertex. This new feature is the geodesic signed distance function (a signed distance function defined only on the surface of the mesh) which defines the geodesic distance from each point on the mesh to the boundary where the head vessels branch off on the aortic arch. By creating this new feature, the branching locations for each vessel can be implicitly defined, thus retaining more information on the original geometry. As with the pre-existing framework, principal component analysis can be used to extract the most dominant geometric features of the vessel in addition to the locations at which branching is most likely to occur.

Table of Contents

List of Figures

List of Abbreviations

BC Boundary Condition

BCA Brachiocephalic Artery

CBCL Cardiovascular Biomechanics Computation Lab

CT Computed Tomography

GPA Generalized Procrustes Analysis

GSDF Geodesic Signed Distance Function

IC Initial Condition

LCCA Left Common Carotid Artery

LSA Left Subclavian Artery

MR Magnetic Resonance

OSI Oscillatory Shear Index

PC Principal Component

PCA Principal Component Analysis

RCCA Right Common Carotid Artery

RSA Right Subclavian Artery

SDF Signed Distance Function

SSM Statistical Shape Modeling

SVD Singular Value Decomposition

TAA Thoracic Aortic Aneurysm

WSS Wall Shear Stress

Chapter 1

Introduction

Aneurysms are characterized by the dilation of a segment of the blood vessel leading to an increased tendency to further inflate, delaminate, or rupture. They can develop in various parts of the body such as the thoracic aorta, abdominal aorta, and cerebral vessels. The focus of this thesis is on a subclass of aortic aneurysms that occur in the thoracic aorta known as thoracic aortic aneurysms (TAA). Though the inflation of the vessel in itself is largely asymptomatic, a rupture or dissection of the affected region is a highly lethal cardiothoracic emergency with a post-operative mortality of up to 25% [4]. Several risk factors such as advanced age, male sex, smoking, a family history of aortic aneurysms, and multiple genetic disorders such as Marfan Syndrome, Loeys-Dietz Syndrome, and vascular Ehlers-Danlos Syndrome have been identified [4]. However, the diagnosis and treatment of TAAs remains challenging. It is estimated that only 5% of TAAs are symptomatic prior to rupture or dissection, and even within symptomatic

cases, more than half of them are not diagnosed until a postmortem examination is performed [5]. Given the lethality of a rupture or dissection, early identification is paramount to improving patient outcomes. Once an aneurysm has been identified, the decision for surgical intervention is determined by metrics such as aortic diameter and growth rate [6]. These metrics, however, are outdated and have been shown to be inadequate at advising clinicians on the necessity of preemptive aortic repair [7–9]. Therefore, metrics that consider additional patient-specific factors are necessary to more reliably determine the necessity of preemptive repair and, ultimately, improve patient outcomes.

Having established the clinical need for a more robust metric by which TAAs can be evaluated, Chapter 2 provides a more detailed discussion of TAAs and the emergence of statistical shape modeling (SSM) as a potential mode of evaluation. Chapter 3 provides a step-by-step explanation of the pipeline proposed in this thesis to augment the current SSM framework for TAAs. The chapter analyzes a set of 24 TAAs using the proposed SSM. Chapter 4 discusses the potential applications for the proposed framework along with its limitations and possible future directions.

Chapter 2

Background

2.1 Anatomy of the Thoracic Aorta

The aorta is the largest artery in the body and serves as a conduit through which the heart supplies the rest of the body with oxygenated blood. It begins at the aortic root, continuing into the ascending aorta, where it loops over the heart and to the left through the aortic arch before passing through the descending aorta into the abdominal region. Three additional vessels originate off of the superior side of the aortic arch – the brachiocephalic artery (BCA), left common carotid artery (LCCA), and left subclavian artery (LSA) – which supply the head, neck, and arms. The thoracic aorta includes the ascending aorta, aortic arch, and descending aorta. A labeled diagram of the thoracic aorta is shown in Figure 2.1.

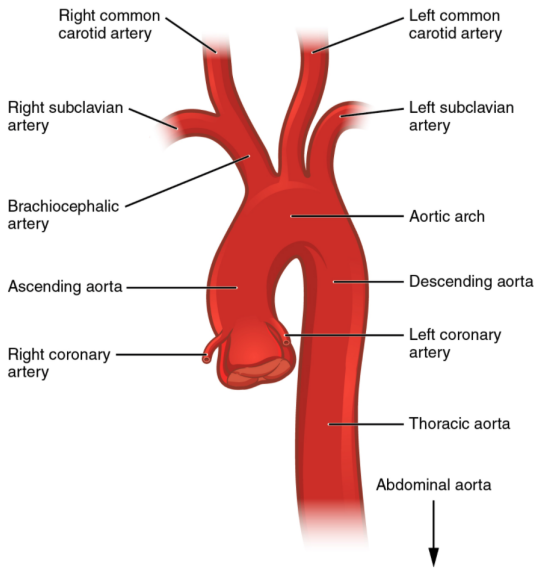

Figure 2.1: Diagram of the thoracic aorta [1]

2.2 Thoracic Aortic Aneurysms

Thoracic aortic aneurysms (TAAs) are a class of aneurysms that occur in the thoracic aorta with an incidence of roughly 10 in a population of 100,000 [5]. Though aneurysms are largely asymptomatic, they increase the risk of either of two events: a rupture, where the wall of the vessel tears completely and causes bleeding inside the body, or a dissection, where the layers of the blood vessel are delaminated, allowing blood to flow into and pool between them. Both are considered an acute cardiothoracic emergency requiring immediate intervention and account for the majority of deaths from TAAs [10].

Multiple risk factors have been identified for TAAs such as age, tobacco use, hypertension, a family history of aneurysms, and various genetic disorders and connective tissue diseases (Marfan syndrome, Ehlers-Danlos syndrome, Loeys-Dietz syndrome) [4,10]. Despite the lethality of aortic aneurysms and the known risk factors, the diagnosis and treatment of TAAs has proven to be challenging. Currently, one of the main modes of treatment for an aortic aneurysm is elective aortic surgery. The decision is based on observations by clinicians and surgeons and a widely followed criteria which recommends surgery for aortic diameters greater than 5.5 cm for non-Marfan patients and 4.5 cm for Marfan patients [11]. This metric, however, has been shown to be inadequate as the majority of patients that suffered aortic dissections had an aortic diameter less than 5.5 cm [7]. A more recent study that evaluated the effectiveness of other metrics such as aortic cross-sectional area to height ratio, concluded that metrics based on basic measurements of the body may be insufficient for advising clinical decisions, and that they may need to be replaced with indices specific to the physics of the aorta being evaluated [9]. Effective strategies for the prevention of TAAs have not yet been found; thus early detection, surveillance, and treatment are paramount to improving patient outcomes [6].

2.3 Computational Simulations of Aortic Aneurysms

A popular approach to address the need for aorta-specific metrics has been the use of computational models of patient-specific geometry. Following advances in medical imaging methods and computation, simulations of the cardiovascular system have become increasingly sophisticated: they have been used not only to understand the underlying pathophysiology, but also to evaluate surgical outcomes and device performance on patient-specific models, encouraging their adoption into the clinical setting [12]. These models are able to provide objective metrics such as wall shear stress (WSS) and the oscillatory shear index (OSI), which can be used to inform clinical decisions regarding aneurysms [13–17].

These models are not without their drawbacks, however, as they are computationally expensive and require individuals with expertise in numerical simulations to obtain physiologically consistent results. Even with the availability of the aforementioned resources, there is not yet a universally-agreed methodology for the assessment of TAAs. Studies have been conducted on the variability of solutions due to user-defined parameters such as boundary conditions (BC), initial conditions (IC), and temporal and spatial discretization schemes amongst a whole host of other parameters, but a consensus on their choices has not yet been reached [18–20].

Open-source simulation software designed specifically for studying patient-specific hemodynamics such as SimVascular [21] and CRIMSON have been developed. Their correct usage, however, as mentioned previously, still requires an understanding of the

underlying physics to select the appropriate solver settings. Given these barriers to accessibility, the adoption of fully-resolved simulations of patient-specific hemodynamics into the clinical setting may be challenging. Therefore there is currently a need for a patient-specific form of evaluating TAAs that can be performed within the time and resource constraints of the clinical setting. One increasingly popular solution has been statistical shape modeling (SSM).

2.4 Statistical Shape Modeling of Aortic Aneurysms

SSMs are "geometric models that describe a collection of semantically similar objects in a very compact way" [22]. When applied to anatomy, they are, put simply, an atlas documenting the variations seen in the geometry of a specific anatomical feature. SSMs have become increasingly popular in biomedical research given their ability to recover intuitive variations in morphological features. They have already been used to analyze the nasal cavity [23], osteoarthritic hips [24], medial meniscus [25], and cranium [26].

TAAs have similarly been studied under the SSM framework [27–29]. These studies demonstrated the ability of SSM to correlate geometric features with clinically relevant metrics such as rupture risk and stratify healthy and pathological vessels using morphological characteristics. These SSMs, however, considered only the ascending and descending portion of the thoracic aorta and removed the head vessels branching off of the aortic arch (BCA, LSA, LCCA). Given the possibility that these branches play a significant role in the mechanics experienced by the aorta, the inclusion of the

branches into the SSM is necessary to reveal additional insights into the morphological characteristics of TAAs.

2.5 Statistical Shape Modeling Framework

The current SSM framework for TAAs is comprised of the following steps:

1. **Image segmentation:** 3D geometry is reconstructed from medical image data
2. **Parent vessel extraction:** Thoracic aorta, also referred to as the parent vessel, is extracted from the original geometry
3. **Mesh parameterization:** Parent vessel mesh is parameterized onto a periodic rectangular parametric domain defined by the longitudinal and circumferential axes
4. **Remeshing:** Parameterized points in the parametric domain are remeshed into a rectangular grid and its associated values are interpolated
5. **Mesh scaling and alignment:** Each of the meshes are aligned to a common coordinate system and scaled
6. **Principal component analysis:** Principal component analysis (PCA) is used to extract the most dominant shape modes from the remeshed geometries
7. **Sample reconstruction:** The original samples can be expressed using the principal components (PCs) as a newly defined coordinate system

8. **Artificial geometry generation:** New geometries can be artificially generated using the SSM

Each of the steps is explained in the following subsections.

2.5.1 Image Segmentation and Model Construction

In the patient-specific modeling of aortic aneurysms, the first step involves model construction from a set of medical data, typically computed tomography (CT) or magnetic resonance (MR) images. For this, packages such as SimVascular [21, 30], Mimics, or other medical image segmentation software can be used to identify the lumen wall in the images. This process may be performed manually, where a user outlines the contours of the lumen, or automatically, where a previously trained model, such as a convolutional neural network, detects the boundaries (Figure 2.2).

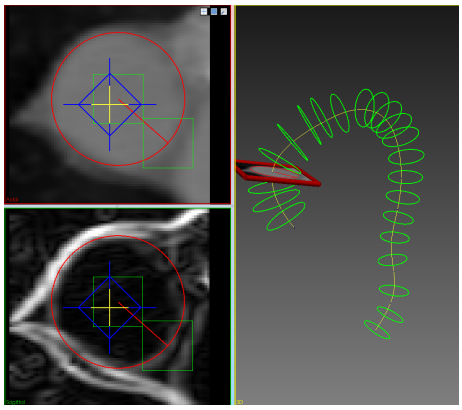

Figure 2.2: Manual segmentation of the thoracic aorta in SimVascular

To add the head vessels into the model, each of their contours must be segmented

as well. Figure 2.3 shows the contours for the LSA and the thoracic aorta.

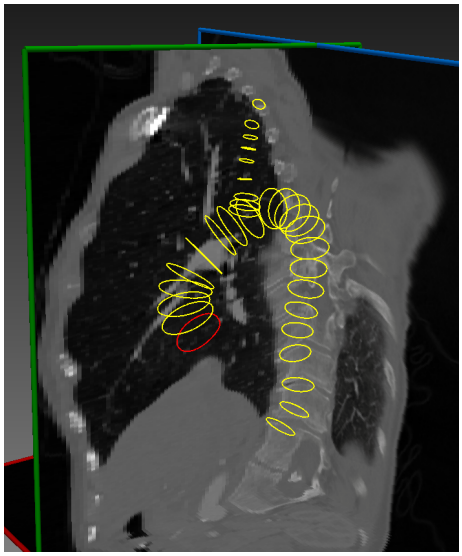

Figure 2.3: Lumen profiles for the thoracic aorta and LSA

Once the contours of the vessels of interest have been segmented, their profiles can be interpolated to produce a 3-dimensional surface model of the patient anatomy (Figure 2.4a). From this, a triangular surface mesh can be created (Figure 2.4b). Once the surface mesh has been created, additional operations may be performed to improve the mesh quality before exporting it for the following steps.

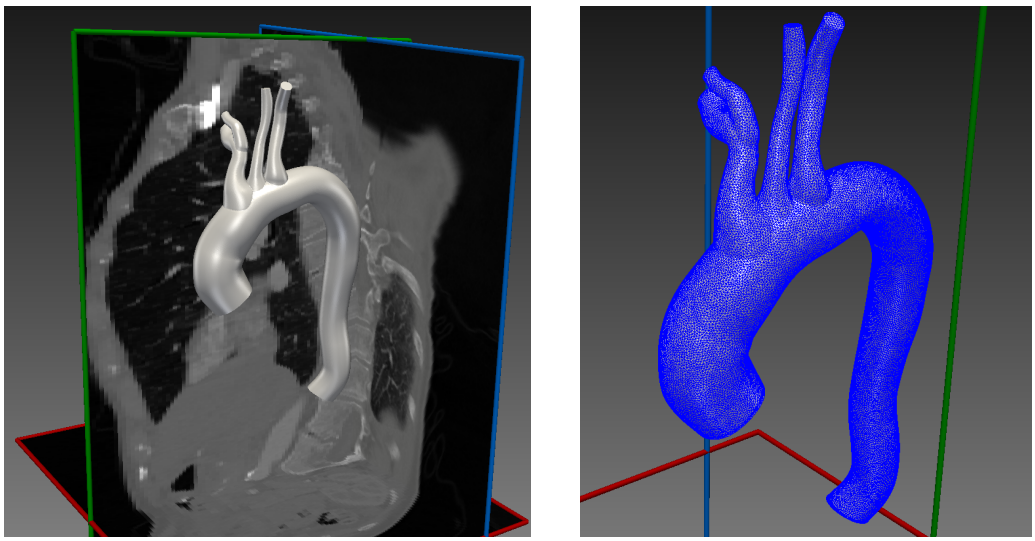

(a) Surface model created from contours

(b) Triangular surface mesh

Figure 2.4: Creation of triangular surface mesh

2.5.2 Parent Vessel Extraction

Once a 3-dimensional model of the thoracic aorta is created, the parent vessel (ascending aorta, aortic arch, and descending aorta) is extracted from the original geometry. This process can be performed manually or programatically. The manual method uses segmentation software such as Mimics or Avizo or with a general mesh editing software such as Meshmixer. The parent vessel can also be extracted programatically using the VMTK software [31]. The two blocks on the right of Figure 2.5 show the results of VMTK's parent vessel reconstruction algorithm on two cerebral aneurysms.

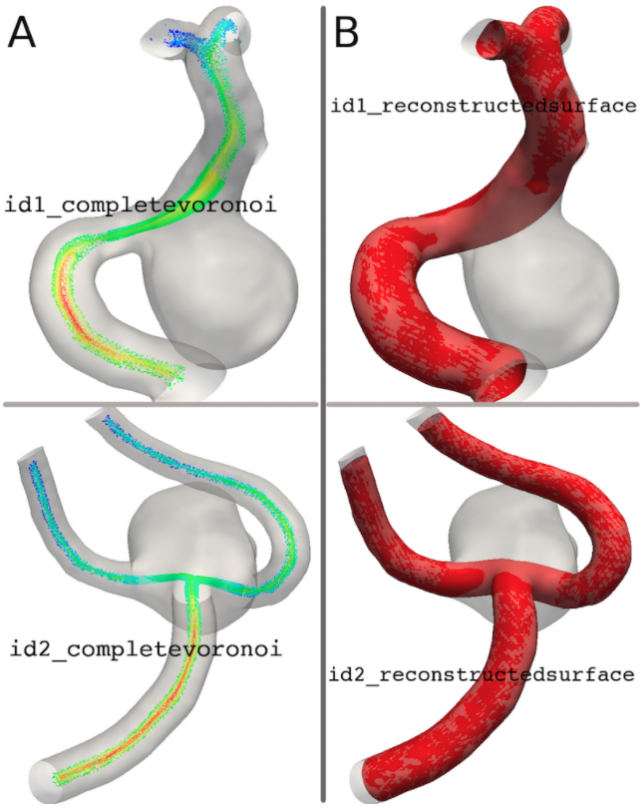

Figure 2.5: Parent vessel extraction of cerebral aneurysms using VMTK [2]

2.5.3 Mesh Parameterization

Mesh parameterization refers to the calculation of a bijective (one-to-one) mapping between any two surfaces of similar topology. In this case, a triangular surface mesh of the parent vessel is parameterized onto a parametric periodic rectangular domain. The original points of the surface mesh $\boldsymbol{x} = [x, y, z]^T \in \mathbb{R}^3$ are mapped to the parametric points $\boldsymbol{u} = [\xi, \eta]^T \in \mathbb{R}^2$. With this parameterization, the coordinate axes are transformed from the canonical basis in $\mathbb{R}^3$ to a longitudinal (η) and circumferential (ξ) axes.

The ξ- and η- axes are analogous to the azimuth (ϕ) and axial coordinate or height (z) in the cylindrical coordinate system, respectively. The radial distance (ρ) in the cylindrical coordinate system can be neglected as the original mesh being parameterized does not have a thickness. With this mapping, the vertices of the parent vessel mesh can be written as a function of the parametric variables:

$$x \equiv x(\xi, \eta) \qquad y \equiv y(\xi, \eta) \qquad z \equiv z(\xi, \eta) \tag{2.1}$$

where $\xi \in [-\pi, \pi)$ and $\eta \in [0, \eta_{\max}]$. Each point in the parametric space corresponds to a point in the original space and vice versa. This parameterization is performed for all parent vessel meshes.

2.5.4 Remeshing

In their original forms, each mesh is composed of a different number of vertices thus resulting in a different number of points in the parametric domain. When building an SSM, each of the points must correspond to the same anatomical landmark across the samples (one-to-one point correspondence). For this a remeshing procedure can be used to interpolate the coordinates of the landmark points for each of the meshes in the parametric domain.

A regular grid with a set number of points in the ξ- and η- axes is initialized and the values of (x, y, z) for each parametric point for each vessel can be calculated using a bilinear interpolation scheme. In doing so, each mesh is now composed of the same number of vertices, with each vertex positioned at the same anatomical landmark.

2.5.5 Mesh Scaling and Alignment

Once the parent vessels have been remeshed, they are scaled and aligned so that the SSM is agnostic to the location, scale, and orientation of the meshes. For this, a method known as Generalized Procrustes Analysis (GPA) can be used [32].

Procrustes Distance

The Procrustes distance is a metric that calculates the similarity (or rather dissimilarity) between two shapes in the form of a distance. Mathematically, the Procrustes distance, d, between shapes $\boldsymbol{X}^{(1)} \in \mathbb{R}^{n\times 3}$ and $\boldsymbol{X}^{(2)} \in \mathbb{R}^{n\times 3}$ is defined as

$$d = \sqrt{\sum_{i=1}^{n}[(x_i^{(1)} - x_i^{(2)})^2 + (y_i^{(1)} - y_i^{(2)})^2 + (z_i^{(1)} - z_i^{(2)})^2]} \tag{2.2}$$

where n is the number of points $x_i^{(j)}$ is the x-coordinate of the i-th point for the j-th shape, and similarly for $y_i^{(j)}$ and $z_i^{(j)}$. The distance is easily generalized to higher and lower dimensions, but Equation 2.2 suffices for shapes in $\mathbb{R}^3$.

Generalized Procrustes Analysis

GPA uses the Procrustes distance to align a set of $K \geq 2$ shapes, each with N points, through the following steps (notation from Liang et al. [29]):

1. Randomly initialize one of the shapes as the reference shape
2. Align all shapes to the reference shape by a similarity transform
3. Calculate the mean shape from the aligned shapes

4. Calculate the Procrustes distance between the mean and reference shape

5. Set the new reference shape to be the mean shape

6. Repeat Steps 2 to 5 until the Procrustes distance calculated in Step 4 is below a set threshold

The mean shape in Step 3 is defined as

$$\begin{aligned}\bar{\boldsymbol{X}} &= [\bar{\boldsymbol{x}}_1, \ldots, \bar{\boldsymbol{x}}_n, \ldots, \bar{\boldsymbol{x}}_N] \\ &= \left[\frac{1}{K}\sum_{k=1}^{K}\boldsymbol{x}_1^{(k)}, \ldots, \frac{1}{K}\sum_{k=1}^{K}\boldsymbol{x}_n^{(k)}, \ldots, \frac{1}{K}\sum_{k=1}^{K}\boldsymbol{x}_N^{(k)}\right] \\ &= \frac{1}{K}\sum_{k=1}^{K}\boldsymbol{X}^{(k)}\end{aligned} \tag{2.3}$$

where $\boldsymbol{X}^{(k)}$ is the k-th shape and $\boldsymbol{x}_n^{(k)} \in \mathbb{R}^3$ is the n-th point of the k-th shape. The solution to the generalized Procrustes problem is determined by minimizing the objective function below

$$\arg\min_{s,R,t} \sum_{k=1}^{K}\sum_{n=1}^{N}\left\|\bar{\boldsymbol{x}}_n - sR\boldsymbol{x}_n^{(k)} - \boldsymbol{t}\right\|^2 \tag{2.4}$$

where s is a scaling factor, R is a rotation matrix, and $\boldsymbol{t}$ is a translation vector.

Orthogonal Procrustes Analysis

It should be noted that a variant of the problem exists, known as the orthogonal Procrustes problem [33]. Whereas in GPA, the shapes undergo a similarity transform (translation, scaling, and rotation) to achieve the optimal alignment (Step 2), the orthogonal Procrustes problem seeks to achieve optimal alignment through rotation only.

The minimization problem is a simpler form of Equation 2.4:

$$\arg\min_{R} \sum_{k=1}^{K} \sum_{n=1}^{N} \left\| \boldsymbol{x}_n - R\bar{\boldsymbol{x}}_n^{(k)} \right\|^2 \quad \text{s.t.} \quad R^T R = I \tag{2.5}$$

2.5.6 Principal Component Analysis

PCA is a fundamental dimension reduction technique in the field of data science [34]. More specifically, it is a method that builds a hierarchical coordinate system that captures the most dominant statistical variations seen in a data set. When used for SSM, it untangles otherwise intertwined morphological variations into independent components. The steps involved in PCA are described below within the context of SSM for TAAs.

The vertices for each vessel are vectorized and entered into individual rows of a matrix $X \in \mathbb{R}^{K \times 3N}$:

$$X = \begin{bmatrix} - & \boldsymbol{X}^{(1)} & - \\ & \vdots & \\ - & \boldsymbol{X}^{(k)} & - \\ & \vdots & \\ - & \boldsymbol{X}^{(K)} & - \end{bmatrix} = \begin{bmatrix} x_1^{(1)} & y_1^{(1)} & z_1^{(1)} & \cdots & x_N^{(1)} & y_N^{(1)} & z_N^{(1)} \\ & \vdots & & & & \vdots & \\ x_1^{(k)} & y_1^{(k)} & z_1^{(k)} & \cdots & x_N^{(k)} & y_N^{(k)} & z_N^{(k)} \\ & \vdots & & & & \vdots & \\ x_1^{(K)} & y_1^{(K)} & z_1^{(K)} & \cdots & x_N^{(K)} & y_N^{(K)} & z_N^{(K)} \end{bmatrix} \tag{2.6}$$

where $x_i^{(j)}$, $y_i^{(j)}$, and $z_i^{(j)}$ are the x-, y-, and z-coordinates of the i-th point of the j-th remeshed vessel, respectively[1]. Once the matrix X has been defined, the data are

[1] The X matrix can be constructed such that, for each column, all the x-coordinates are listed followed by all the y- and z-coordinates as long as the inverse of the reshaping operation is used to reconstruct the matrix.

shifted such that they are centered around the origin, resulting in the mean-subtracted data B:

$$B = X - \bar{X} = X - \mathbf{1} \otimes \bar{\boldsymbol{x}}^T \tag{2.7}$$

where $\mathbf{1} \in \mathbb{R}^{3N}$ is a column vector of ones, $\otimes$ is the outer product, and $\bar{\boldsymbol{x}} \in \mathbb{R}^{3N}$ is the column-wise mean of X. Then, the covariance matrix C of the rows of B is calculated:

$$C = \frac{1}{K-1} B^T B \tag{2.8}$$

Next, the eigendecomposition of C is calculated

$$C = V \Lambda V^T = \sum_{i=1}^{r} \lambda_i v_i v_i^T \tag{2.9}$$

where the columns of V are the eigenvectors and Λ is a diagonal matrix containing the eigenvalues λ_i of C, and $r = rank(B)$. These eigenvectors form the newly constructed basis, also known as the PCs[2]. Finally, the projection of the original data onto these PCs, commonly referred to as the PC scores[3], are calculated as

$$T = BV \tag{2.10}$$

where each row represents the projection of the original data point onto the span of the PCs. In practice, the PCs can be obtained by simply calculating the singular value decomposition (SVD) of the mean-centered data matrix B:

$$B = U \Sigma V^T \tag{2.11}$$

[2]The literature varies in its nomenclature for terms used in PCA. Others may refer to the PCs here as principal axes or principal directions.

[3]In the case that the previously mentioned convention is used, PC scores here are equivalent to PCs.

where the columns of V are the PCs and the singular values σ_i from the diagonal matrix Σ capture the variance. For the SVD-based method, the projection of the original data onto the span of the PCs using the factored matrices is given by

$$BV = U\Sigma V^T V = U\Sigma \tag{2.12}$$

The variance captured by the first r PCs, also known as the cumulative energy, is calculated as

$$\frac{\sum_{i=1}^{r} \lambda_i}{\sum_{i=1}^{K} \lambda_i} = \frac{\sum_{i=1}^{r} \sigma_i^2}{\sum_{i=1}^{K} \sigma_i^2} \tag{2.13}$$

Equation 2.13 is used to determine the number of PCs to be kept by selecting the first r PCs such that the cumulative energy satisfies a threshold (i.e. 90% or 0.9).

2.5.7 Sample Reconstruction

With these PCs V_i, each of original vessels $\boldsymbol{X}^{(k)}$ can be approximately reconstructed as a linear combination of the first m PCs. Let $\tilde{V}$ be a matrix composed of the first m columns of V; then the approximate reconstruction of the original set of vessels X using the first m PCs is

$$X \approx \bar{X} + B\tilde{V}\tilde{V}^T \tag{2.14}$$

As specified in Equation 2.13, the total variation captured increases as m increases. Therefore a larger m provides a more accurate reconstruction with the original samples being returned when $m = r$ in Equation 2.14.

2.5.8 Artificial Geometry Generation

Just as the original vessels can be approximately reconstructed, new vessel geometries can be synthesized by taking linear combinations of the first m PCs.

$$X^{(\text{new})} = \bar{X} + \sum_{i=1}^{m} c_i \sqrt{\lambda_i} V_i \quad \text{where } m \leq r \tag{2.15}$$

The c_i are a set of parameters that can be modified to vary the contribution of each PC to the final geometry. As the value of c_i is analogous to the standard deviation from the mean shape for a given PC, typical values may range from -2 to 2 [29].

2.6 Limitations of the Current Framework

In its current form, a major limitation of the SSM framework is the inability to incorporate information on the head vessels branching off of the aortic arch. In the mesh parameterization step, the input mesh (mesh to be parameterized) must be homeomorphic to a cylinder, and thus the branches must be removed and the remaining holes must be closed prior to the parameterization. Given the possible effect of these branches on the mechanics of the thoracic aorta, the inclusion of the branches is critical to further understanding the morphological characteristics of TAAs. To address this issue, this thesis presents a method to embed information regarding the head vessels into the preexisting SSM framework whilst satisfying the homeomorphicity requirement.

Chapter 3

Methods & Results

Given that this thesis presents a pipeline for the SSM of TAAs, the methods and results section have been consolidated into a single section to present the implementation and results of each step chronologically. The proposed SSM framework augments the existing framework with the addition of a new feature in the form of a geodesic signed distance function (GSDF) to implicitly define the locations of the head vessels. The framework was implemented in the ssmtk package written in Python [35]. Many of the steps outlined below were run on Jupyter Notebooks to produce images [36]. The plotting packages Plotly [37], matplotlib [38], and Bokeh [39] were used for plotting.

3.1 Data Overview

Medical imaging data of TAAs were provided by multiple sources. Below is a description of the data received from each source.

3.1.1 OSMSC vessels

Meshes of the thoracic aorta were provided by the Cardiovascular Biomechanics Computation Lab (CBCL) at Stanford University (Figure 3.1). In total, there were 24 meshes of the thoracic aorta beginning at the aortic root and ending proximal to the renal arteries. Each vessel also included the three head vessels branching off of the aortic arch: the innominate artery, which branches into the right common carotid artery (RCCA) and right subclavian artery (RSA), LCCA, and LSA. The meshes were provided in VTP format [40].

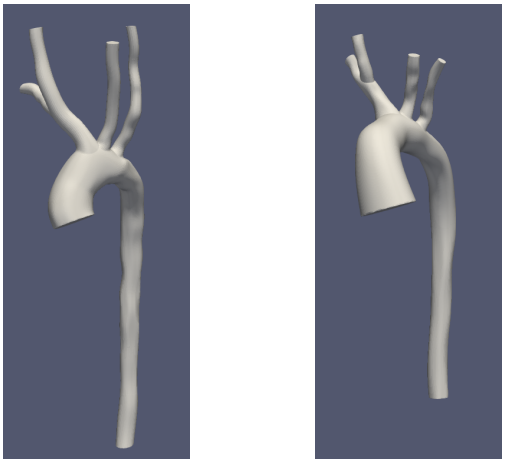

(a) 0063_1001 (b) 0075_1001

Figure 3.1: Original meshes of the thoracic aorta provided by the CBCL

3.1.2 Washington University in St. Louis vessels

Professor Jessica Wagenseil at Washington University in St. Louis provided MR images of the thoracic aorta. In total, medical image data for 165 patients with Marfan syndrome were provided in DICOM format [21]. Image segmentation was performed with SimVascular to construct 3D models of the vessels.

3.1.3 University of Minnesota vessels

Additional imaging data of the thoracic aorta was provided by Dr. Rochus Voeller at the University of Minnesota. Similar to the vessels from Washington University, these vessels were provided in DICOM format. Image segmentation was performed using SimVascular as well [21]. Though 79 separate scans were provided, only 14 provided could be converted into usable 3D surface models.

3.1.4 Final Dataset

Though models of the thoracic aorta were provided by multiple sources, only the OSMSC vessels were used in the construction of the SSM. The quality of the models constructed from the Washington University and University of Minnesota vessels were poor compared to the OSMSC vessels. Since this thesis aims to present a new methodology for the SSM of TAAs, as opposed to the analysis of TAAs using SSM, only the OSMSC vessels were used in the final construction of the SSM.

3.2 Parent Vessel Extraction

The parent vessel of each vessel was created by removing elements of the original mesh if they were on the branching vessels as opposed to the parent vessel using MeshMixer [41]. Once removed, the surface was smoothed such that the curvature of the manipulated surface was consistent with the surrounding mesh. The extracted parent vessel (blue) and original vessel (gray) for two vessels are shown in Figure 3.2.

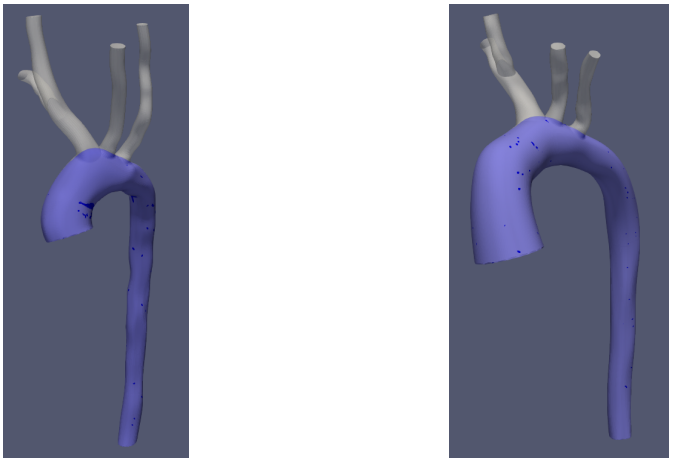

(a) 0063_1001 (b) 0075_1001

Figure 3.2: Parent vessels (blue) of original vessels (gray).

Parent vessel extraction was also performed using the automated method introduced in Section 2.5.2. However, the method failed to reconstruct the parent vessel accurately. Thus the manual method was used for the extraction of all parent vessels.

3.3 Parent Vessel Mesh Parameterization

Once the parent vessels were extracted, each parent mesh was parameterized onto a periodic rectangular parametric domain using VMTK [31]. The parametric domain was defined by the ξ and η axes, which represented the circumferential and longitudinal axes of the vessels, respectively. Note that the periodicity applies only to the circumferential axis. The longitudinal coordinate is defined as the distance along the centerline from the most proximal point on the vessel and the circumferential coordinate is the angular position of the vertex with respect to the centerline (Figure 3.3).

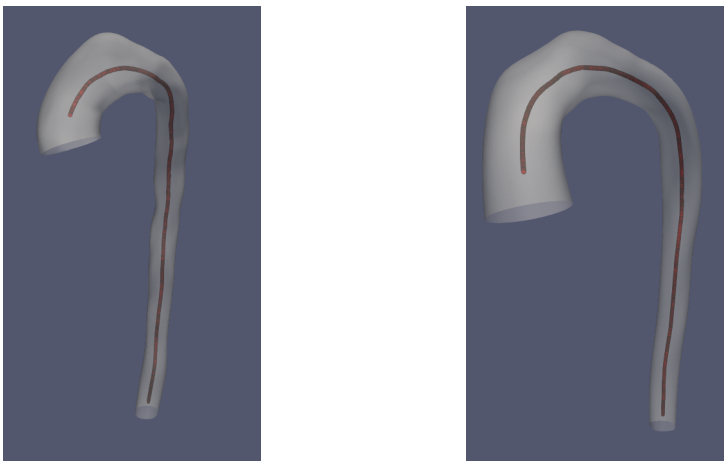

(a) 0063_1001 (b) 0075_1001

Figure 3.3: Parent vessel centerline

In doing so, surface-based quantities (including vertex coordinates in the physical domain) for various geometries can be compared in a shared parametric space [42]. The parameterization of two parent vessel meshes with the surface color corresponding to the

point's parametric coordinate is shown in Figure 3.4. The abscissa metric and angular metric refer to the longitudinal (η) and circumferential (ξ) axes, respectively.

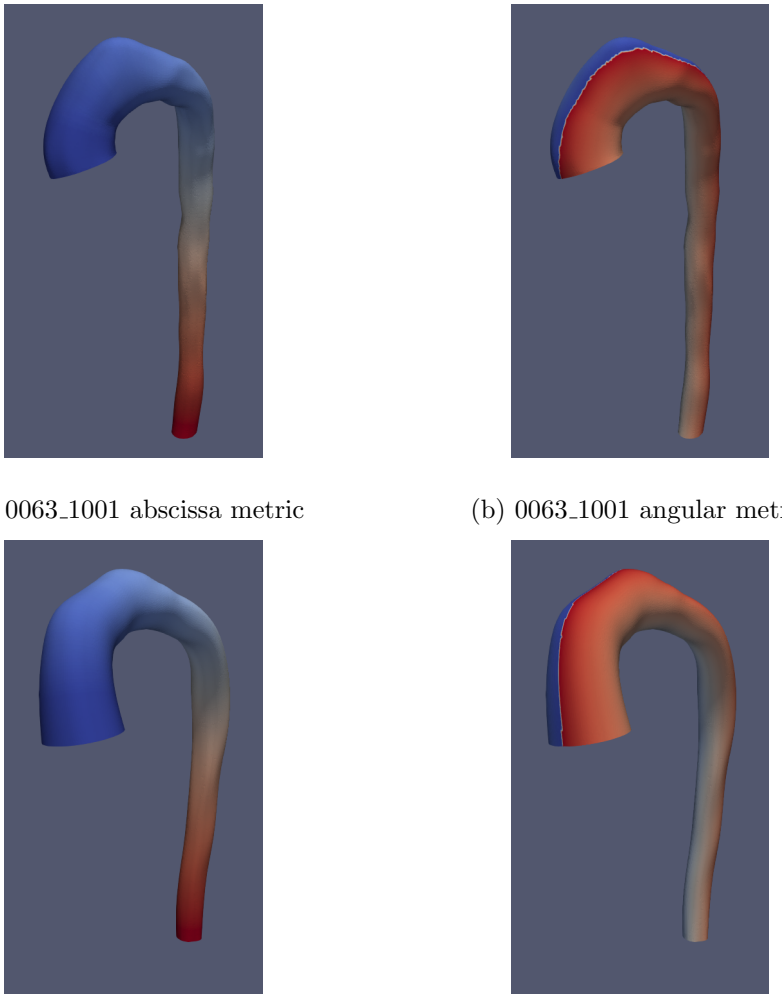

(a) 0063_1001 abscissa metric

(b) 0063_1001 angular metric

(c) 0075_1001 abscissa metric

(d) 0075_1001 angular metric

Figure 3.4: Parameterization of parent vessels (physical domain)

The longitudinal axis (η) begins at the aortic root and ends at the distal end of the descending aorta (Figures 3.4a and 3.4c). A similar consistency across the samples is

observed with the circumferential axis (ξ), as the most negative value, $-\pi$, corresponds to what would be the most lateral point on the aortic root and increases in the clockwise direction (Figures 3.4b and 3.4d). The parameterized coordinates can similarly be plotted in the parametric domain (Figure 3.5).

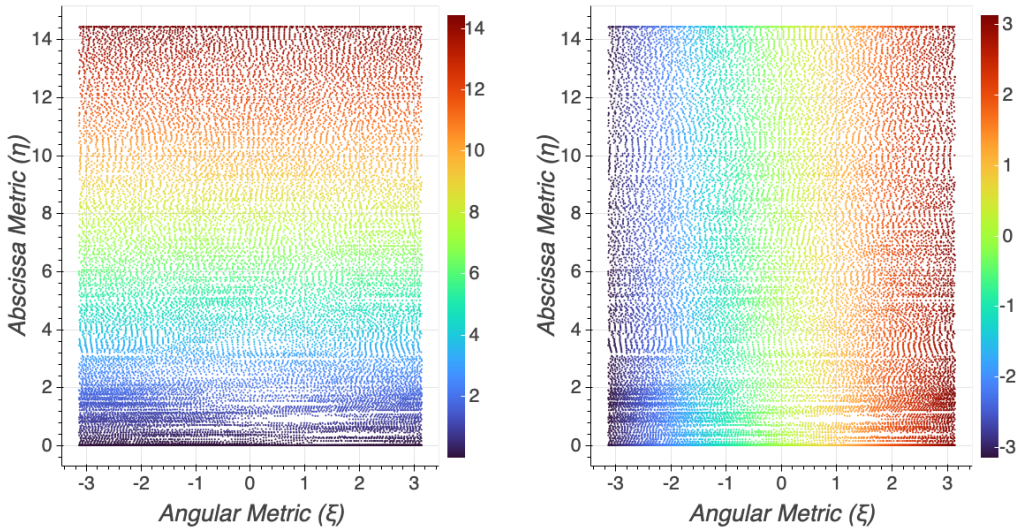

(a) 0063_1001 abscissa metric

(b) 0063_1001 angular metric

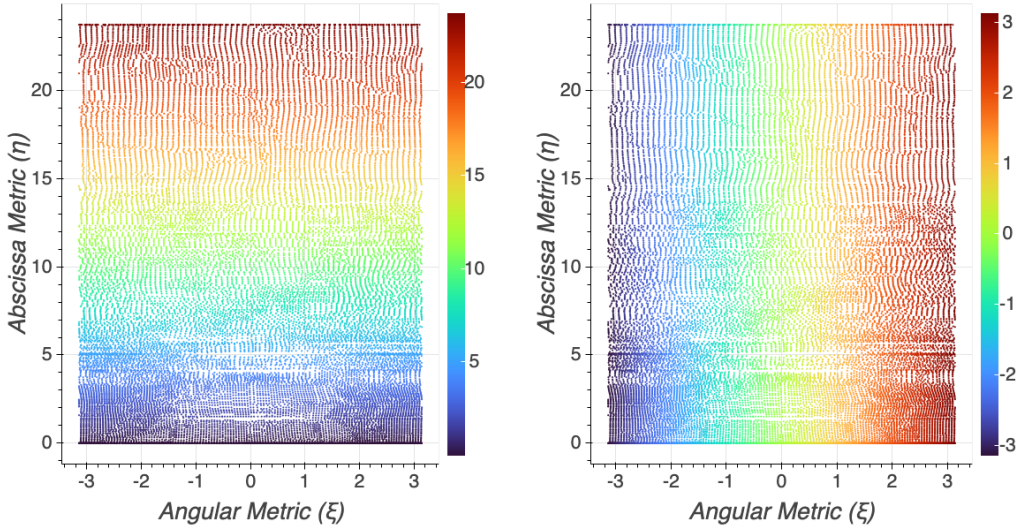

(c) 0075_1001 abscissa metric

(d) 0075_1001 angular metric

Figure 3.5: Parameterization of parent vessels (parametric domain)

Figures 3.5b and 3.5d clearly show that the angular metric for each vessel ranges from $-\pi$ (blue) to π (red). The abscissa metric, though limited to nonnegative values for

all vessels, did not have consistent ranges as each vessel had a different centerline length (Figures 3.5a and 3.5c). The maximum η coordinate for each vessel is semantically similar as they represent the most distal point on the descending aorta. Therefore, the η-values for each vessel were normalized such that the $\eta_{\max}$ for each vessel was the same.

3.4 Branch Mapping

Following the extraction of the parent vessel, elements of the parent vessel mesh located in the branching regions were removed, leaving the parent vessel mesh with holes at the locations of the branches (Figure 3.6). This was performed to allow the subsequent identification of the boundaries of the branching head vessels on the aortic arch.

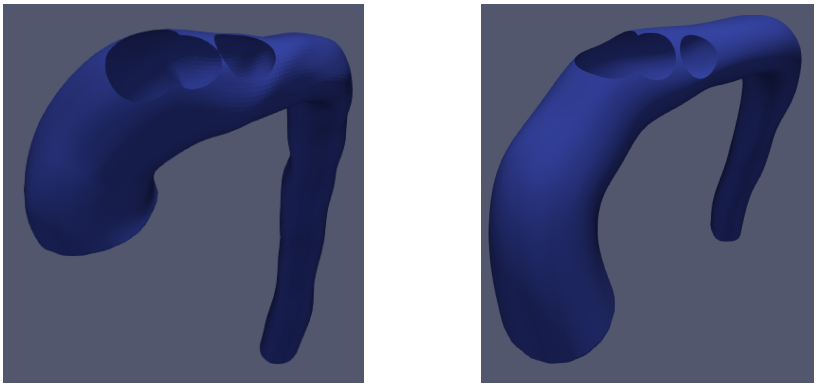

(a) 0063_1001 (b) 0075_1001

Figure 3.6: Parent holes with elements in the branching region removed.

Standard mesh processing packages were able to detect holes in the mesh, as many applications require meshes to be watertight. By exploiting this feature, the indices of

the vertices on the boundaries were identified (Figure 3.7).

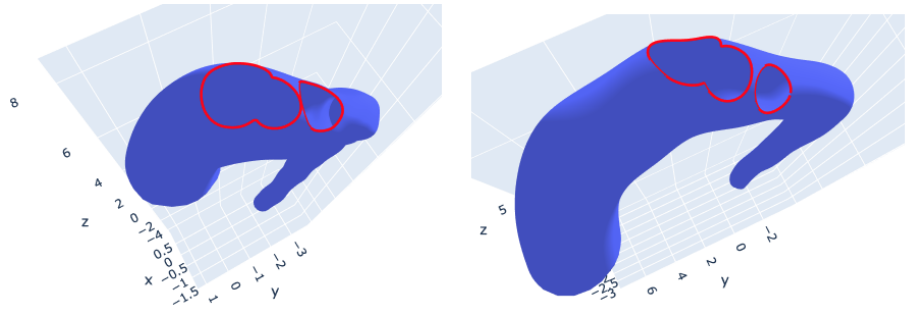

(a) 0063_1001 (b) 0075_1001

Figure 3.7: Parent mesh with edges on the boundaries of the branch holes highlighted.

These boundary vertices were then mapped onto the surface of their corresponding parent vessel mesh. Because the surface of the parent vessel was modified to fill the hole, the parent vessel mesh and the parent vessel mesh with holes do not align perfectly for the remaining elements (Figure 3.8).

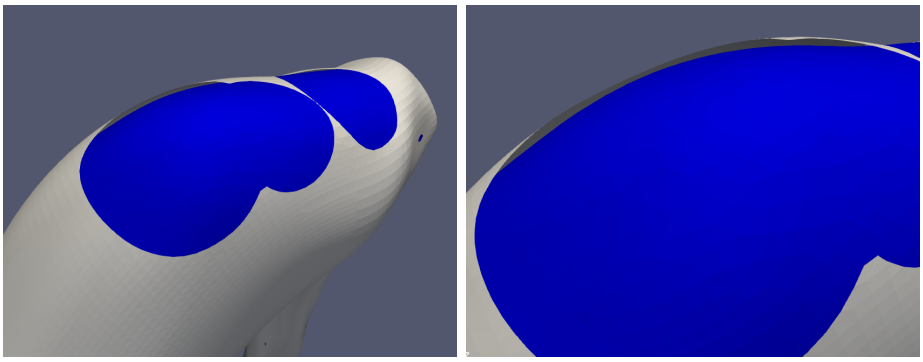

(a) Areas of discrepancy for 0063_1001 (b) Zoomed-in view of the error

Figure 3.8: Discrepancy between the coordinates of the remaining points on the parent vessel mesh with holes (gray) and original parent vessel mesh (blue)

To address this, boundary vertices were mapped onto the parent vessel mesh by finding each of the boundary vertices' nearest neighbor. In doing so, the branching regions could be identified on the surface of the parent vessel mesh (Figure 3.9). The indices of the mapped boundary vertices on the parent vessel mesh were identified in addition to their coordinates.

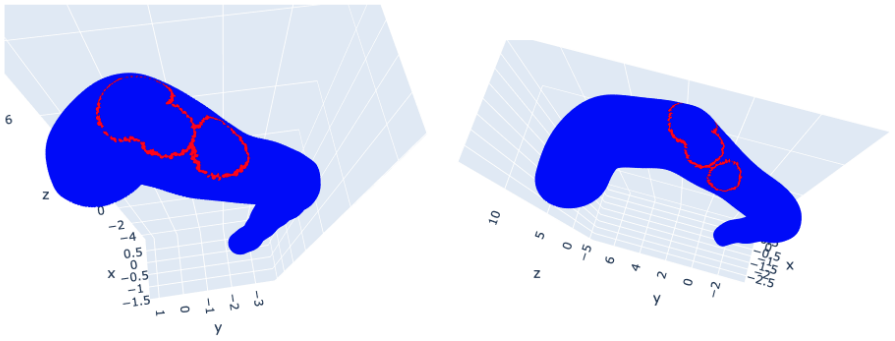

(a) 0063_1001 (b) 0075_1001

Figure 3.9: Boundaries of branch holes (red) mapped onto the surface of the parent vessel (blue)

Though this step results in slight inaccuracies on the origins of the head vessels, the mapping of the boundary vertices allowed the construction of the SSM without violating the homeomorphicity constraint.

3.5 Scaling

Instead of using GPA for the scaling, translation, and rotation of the mesh for alignment, a centerline length-based scaling law was first used to isotropically scale the meshes. The centerlines of the parent vessels were extracted, and their lengths were calculated as the sum of the Euclidean distances between each successive point on the centerline. Once the centerline length was calculated for each vessel, the meshes were scaled in one of two ways:

1. Average centerline length: scaled such that each vessel has a centerline length equal to the average centerline lengths of the original parent vessels

2. Specified centerline length: scaled such that each vessel has a centerline length equal to a user-specified value

Because the original vessels were obtained from patients of various ages, centerline lengths varied considerably across the vessels. If the vessels generated using the SSM were to be used in computational studies, parameters such as BCs and material properties are more readily available for the adult population; and for this reason, the second scaling method was used to scale all the meshes to the average adult centerline length observed in the data. Shown below are examples of isotropic scaling on the parent vessels (Figure 3.10).

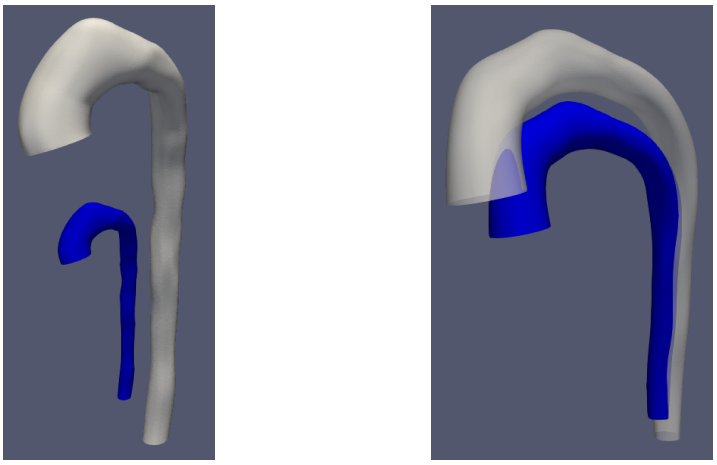

(a) 0063_1001 (b) 0075_1001

Figure 3.10: Comparison of original (blue) and scaled (gray) parent vessel meshes

3.6 Geodesic Signed Distance Function

The geodesic signed distance function (GSDF) combines two concepts from computational geometry: the geodesic distance and the signed distance function (SDF).

3.6.1 Geodesic Distance

Geodesic distance is defined as the length of the shortest path between two points on a surface. Unlike the traditional notion of distance wherein the points can exist anywhere, geodesic distance is limited to points that exist on a surface. Figure 3.11 shows level-sets of the geodesic distance from a point on the back of the Stanford bunny. The black lines represent level-sets of the geodesic distance.

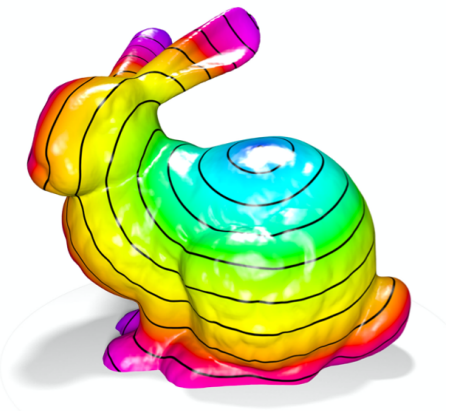

Figure 3.11: Heat map showing the geodesic distance of a given point on the surface of the mesh from a point on the back of the bunny [3].

3.6.2 Signed Distance Function

The SDF is an implicit function that determines the distance of a given point x to the boundary of a shape Ω, where the sign is determined by whether the point is on the interior or exterior of the boundary (Equation 3.1). If the point is inside the shape, the distance is negated, otherwise it remains positive[1].

$$f(x) = \begin{cases} -d(x, \partial\Omega) & \text{if } x \in \Omega^o \\ 0 & \text{if } x \in \partial\Omega \\ d(x, \partial\Omega) & \text{if } x \in \Omega^c \end{cases} \tag{3.1}$$

where $\partial\Omega$ is the boundary of Ω, Ω^o is the interior of the boundary Ω, and Ω^c is the exterior of the boundary Ω. For a given point x, $d(x, \partial\Omega)$ is the distance to the closest point ω on the boundary $\partial\Omega$ (Equation 3.2).

$$d(x, \partial\Omega) = \min_{\omega \in \partial\Omega} \|x - \omega\| \tag{3.2}$$

where $\|\cdot\|$ is a metric, typically the Euclidean distance. Figure 3.12 shows an example of an SDF for a simple shape in 2D where the contours represent level-sets of the SDF.

[1] Other common convention is to negate the distance if the point is on the exterior. This thesis uses the SDF where sign is negative if inside the shape.

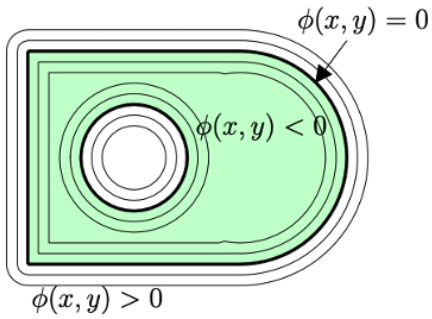

Figure 3.12: SDF for a shape in 2D. Points in the green region have a negative signed distance and points in the white region have a positive signed distance.

The SDF can easily be extended to an arbitrary number of dimensions, most notably to 3D as it implicitly defines a surface – one such example being the Stanford bunny (Figure 3.13). The SDF returns a negative value if the point is inside the mesh, a positive value if outside the mesh, and zero if on the surface of the mesh. The key is to note that the locations at which the signed distances are defined can be chosen without consideration for the underlying geometry. As such, the SDF can be defined with varying resolutions based on the desired accuracy and resolution of the reconstructed surface.

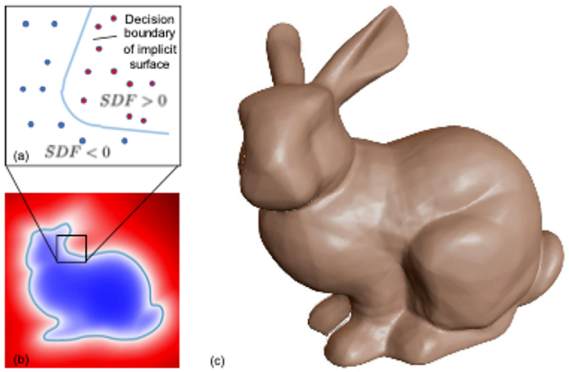

Figure 3.13: Cross-sectional view of the signed distance function of the Stanford bunny.

3.6.3 Calculation of the Geodesic Signed Distance Function

By combining the geodesic distance with the SDF to form the GSDF, the boundary of an arbitrary shape Ω on the surface of a mesh $\mathcal{S}$ can be implicitly defined (Equation 3.3). The definition is similar to that of Equation 3.1, except that the function is defined only on the surface $\mathcal{S}$.

$$f(x : x \in \mathcal{S}) = \begin{cases} -d(x, \partial\Omega) & \text{if } x \in \Omega^o \\ 0 & \text{if } x \in \partial\Omega \\ d(x, \partial\Omega) & \text{if } x \in \Omega^c \end{cases} \tag{3.3}$$

where $d(x, \partial\Omega)$ is the geodesic distance from x to the boundary $\partial\Omega$ on the surface $\mathcal{S}$.

The calculation of the GSDF is comprised of three steps:

1. *Calculate the geodesic distance for every vertex on the surface mesh to a boundary defined on the mesh surface*

Pycortex, a Python module originally developed for the visualization of fMRI and other volumetric neuroimaging data on cortical surfaces, was used in the calculations of geodesic distances [43]. More specifically, the `Surface` class has a method called `geodesic_distance`, which calculates the geodesic distance of each vertex on the surface to a specified collection of vertices on the surface (Figure 3.14). At this point, the geodesic (unsigned) distance function (GDF) is calculated.

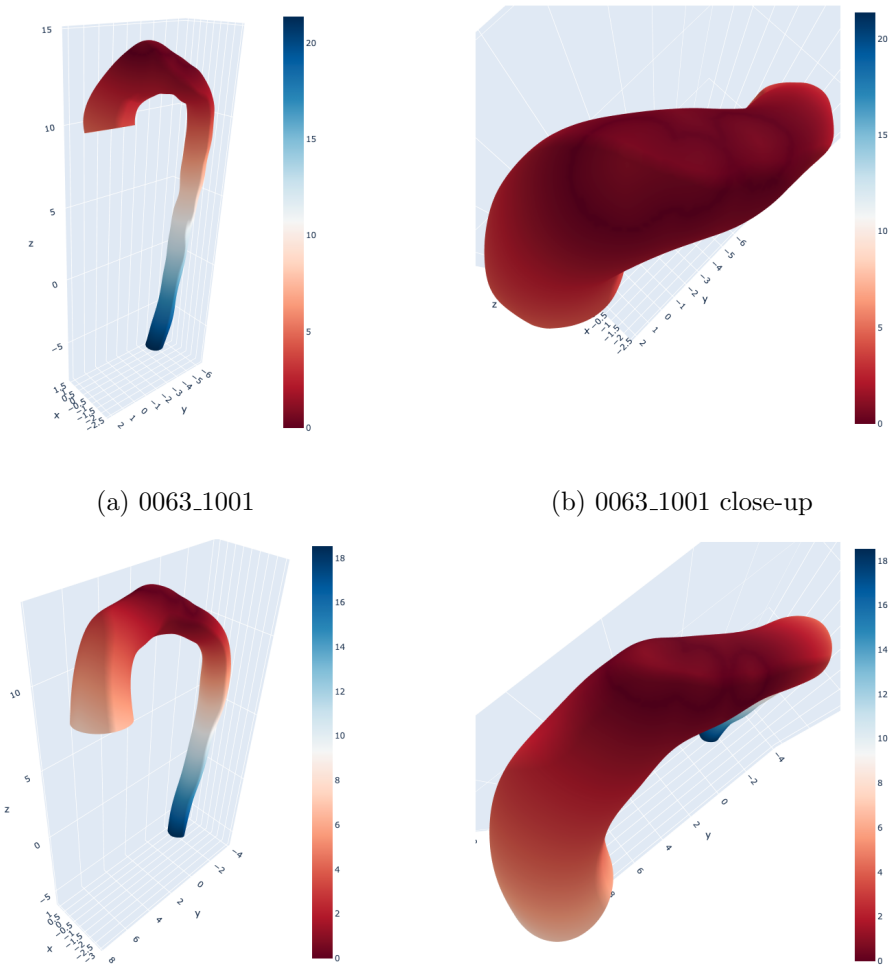

(a) 0063_1001

(b) 0063_1001 close-up

(c) 0075_1001

(d) 0075_1001 close-up

Figure 3.14: Geodesic (unsigned) distance function in the physical domain

The boundary can be seen as the darkest regions on the superior side of the aortic arch (Figures 3.14b and 3.14d). The GDF can similarly be plotted in the parametric domain (Figure 3.15). The black points in the bottom half of the plots are the zero level-sets of the GDF and are the parametric coordinates of the

boundaries of the head vessels.

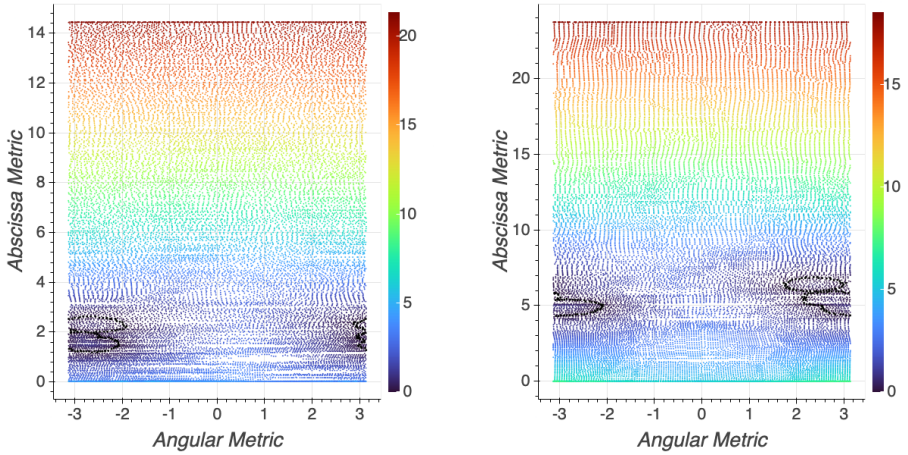

(a) 0063_1001 (b) 0075_1001

Figure 3.15: Geodesic (unsigned) distance function in the parametric domain

2. *Determine the membership of each vertex based on whether it is inside or outside of the boundary*

   To convert the GDF into the GSDF, the membership of every point relative to the boundary is needed. This procedure can more easily be performed in the parametric domain as it is a Euclidean space. To account for the periodicity of the ξ-axis in the parametric domain, all the points were shifted by a value ξ_{shift} such that the boundaries do not cross over the edges of the domain (Figure 3.16).

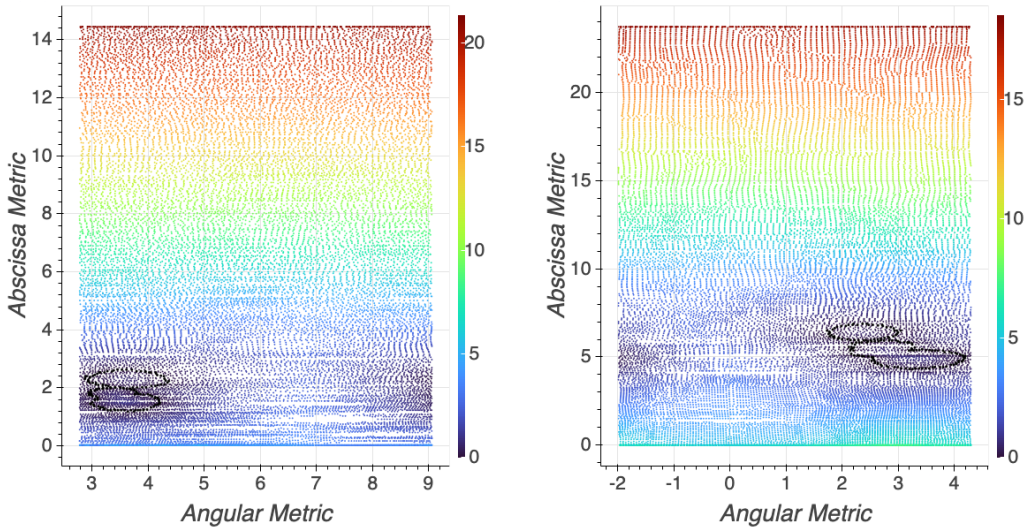

(a) 0063_1001 (b) 0075_1001

Figure 3.16: Shifted geodesic distance function in the parametric domain

Once shifted, the problem of determining the membership of the points was treated as if it were being performed in a non-periodic domain. Using the ordered list of the indices of vertices defining the boundaries from 3.4, polygons were defined in the parametric domain and were used to determine vertex memberships. The membership function m can be expressed as a piecewise function (Equation 3.4). The function returns -1 if the point is inside the boundary and 1 if the point is

outside the boundary. The function returns 0 if the point is on the boundary[2].

$$m(x) = \begin{cases} -1 & \text{if } x \in \Omega^o \\ 0 & \text{if } x \in \partial\Omega \\ 1 & \text{if } x \in \Omega^c \end{cases} \tag{3.4}$$

The function was implemented using the `Path` module from matplotlib [44]. Points inside and outside the boundary are shown in yellow and purple, respectively (Figure 3.17).

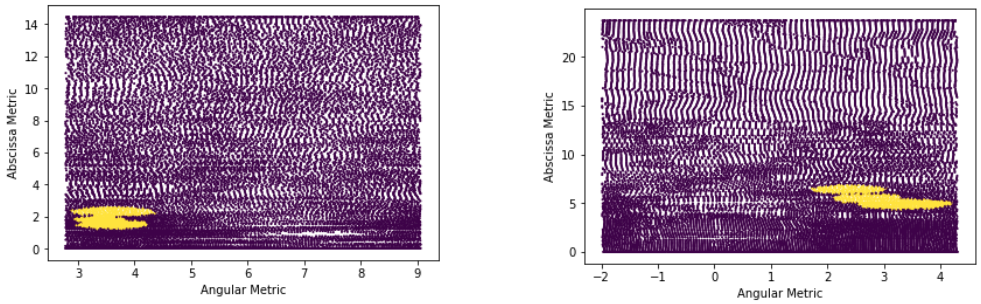

(a) 0063_1001 (b) 0075_1001

Figure 3.17: Membership of points in shifted parametric domain

Once the membership was determined in the shifted domain, the points were shifted back by the ξ_{shift} calculated previously (Figure 3.18).

[2]In reality, the membership function does not need to be defined for $x \in \partial\Omega$ as the GDF is zero and its membership will not affect its corresponding value for the GSDF. However, for the sake of completeness, it is defined here.

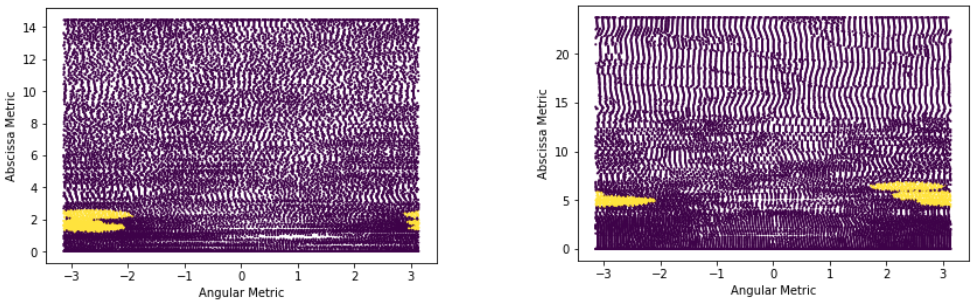

(a) 0063_1001 (b) 0075_1001

Figure 3.18: Membership of points in parametric domain

3. *Negate the geodesic distances for vertices inside the boundary*

The GDF for a point can be converted into the GSDF by negating its value if the point is inside the boundary (Equation 3.5).

$$\mathrm{GSDF}(x) = m(x) \cdot \mathrm{GDF}(x) \tag{3.5}$$

The GSDF plot in the parametric space contains a small region of negative values indicating the location of the head vessels (Figure 3.19). The difference compared to Figure 3.15 is difficult to see, however, the colorbars for the GSDF plots extend to negative values, whereas the GDF plots do not.

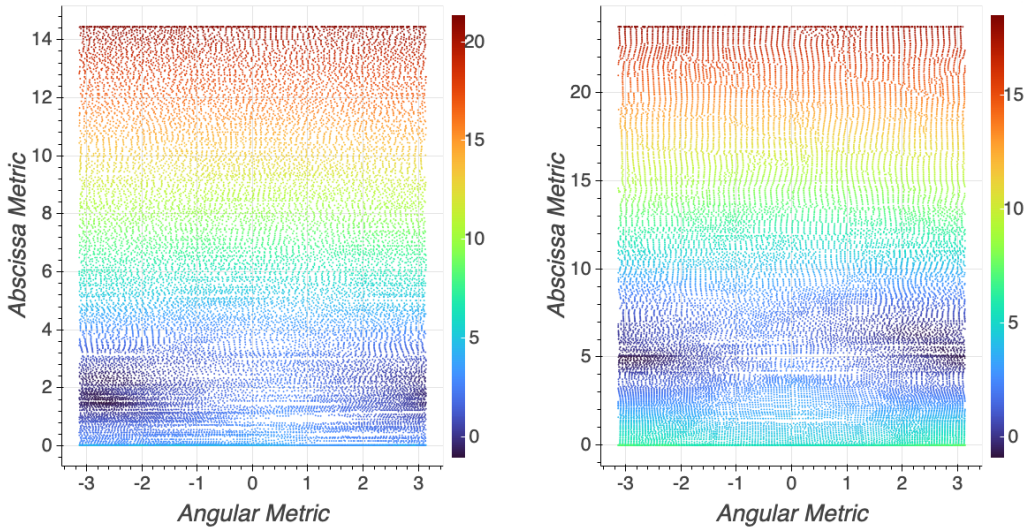

(a) 0063_1001 (b) 0075_1001

Figure 3.19: Geodesic signed distance function in the parametric domain

The sign change is much easier to see in the physical representation (Figure 3.20). Note that the plots' color schemes have been modified such that the zero-level set corresponds to white. The red region comprises of vertices with a negative GSDF value, thus they are on the interior of the boundary, and vice versa for the blue region.

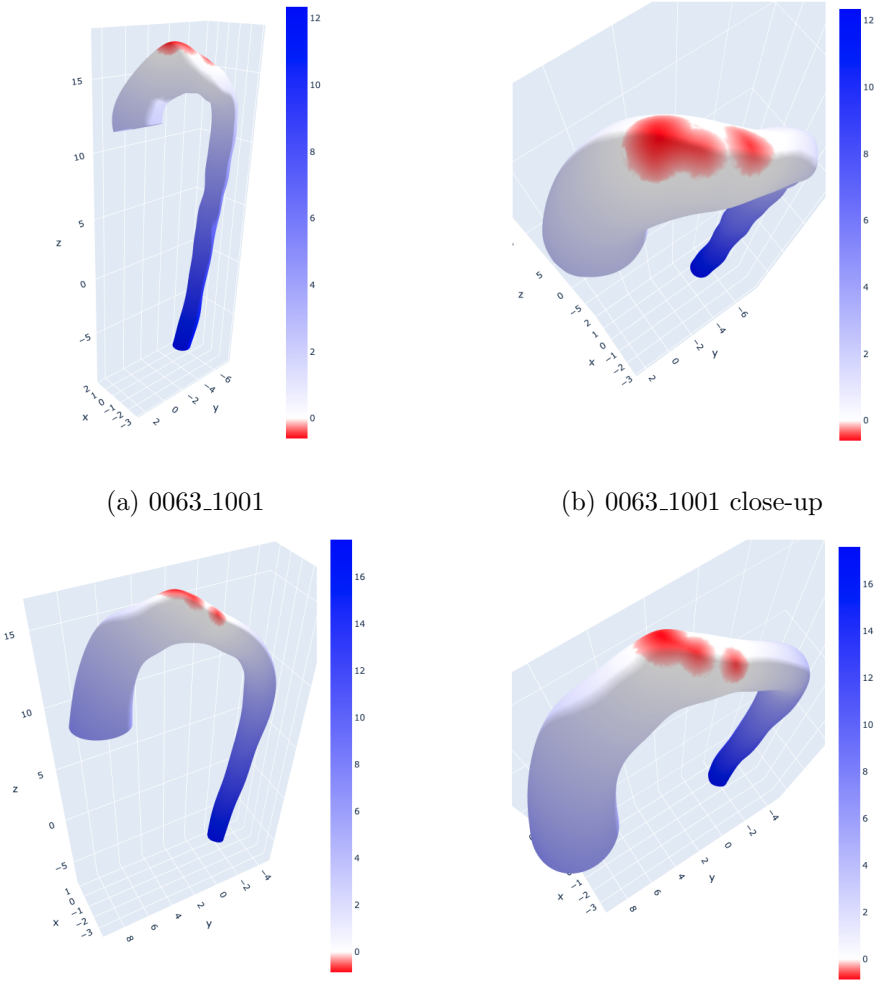

(a) 0063_1001

(b) 0063_1001 close-up

(c) 0075_1001

(d) 0075_1001 close-up

Figure 3.20: Geodesic signed distance function in the physical domain

3.7 Remeshing

Up to this point, each mesh was comprised of a different number of vertices. As discussed in 2.5.4, each vessel must be remeshed to a common parametric grid with the

same number of vertices to establish a point-to-point correspondence for anatomical landmarks across the samples. First, a rectangular grid of vertices was initialized based on the bounds of the original (ξ, η) coordinates for each mesh (Figure 3.21). Since the original meshes had 20,000 to 60,000 vertices, the grid was initialized to have 100 evenly spaced points in each axis so that the number of remeshed vertices (10,000) would be on the same order of magnitude as the number of vertices in the original meshes[3]. In addition, increasing the number of vertices in each axis increases the number of operations quadratically; however, they were found not to have an effect on the accuracy of the remeshed vessels.

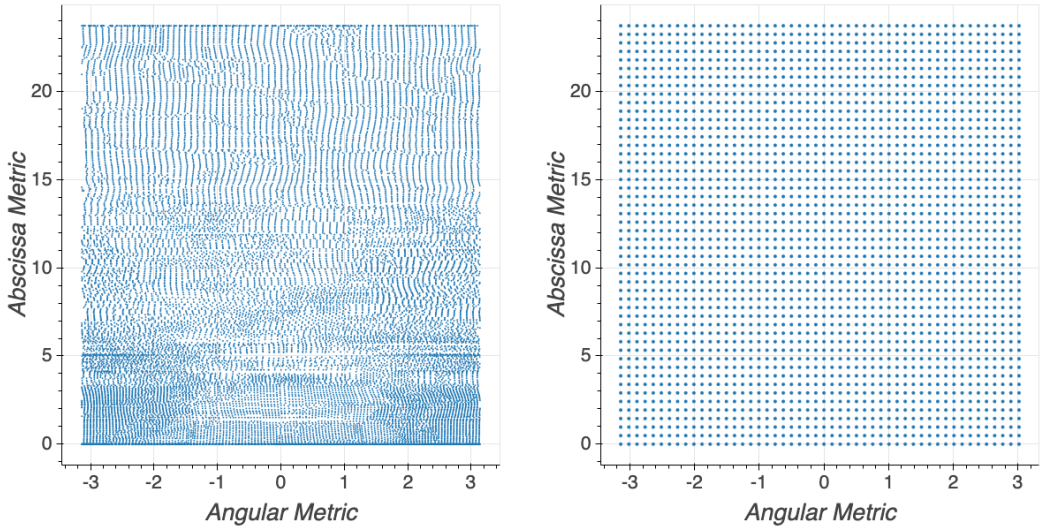

(a) Original parameterized points. (b) Remeshed parameterized points

Figure 3.21: Remeshing of parameterized points onto a rectangular grid (50-by-50) in the parametric domain

[3]The grid in Figure 3.21 has fewer points to provide a clearer visualization of the remeshed grid

The $(x, y, z, G(x, y, z))$ values of the remeshed parametric points were calculated using a multivariate interpolation scheme (`griddata`) from SciPy [45]. The remeshing procedure was repeated for every vessel with the same remeshed grid. Not only does the remeshing establish correspondence between individual shapes, it also fits the data to a regular grid, allowing for a better visualization of the GSDF as shown in Figure 3.22.

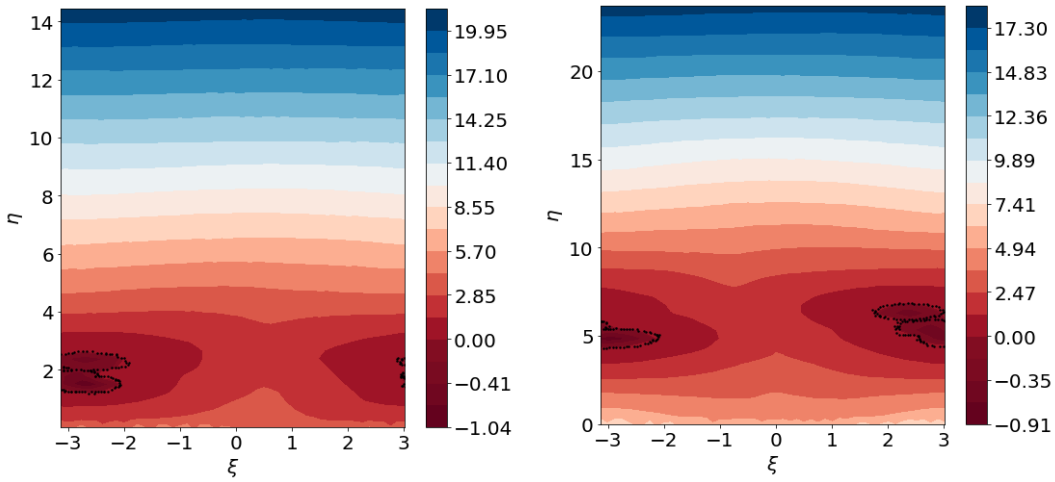

(a) 0063_1001 (b) 0075_1001

Figure 3.22: Contour plot of remeshed GSDF in the parametric space

The remeshing procedure modifies the original points such that the vessel surface is composed of a succession of ring-like contours where each ring corresponds to a level-set of η. This is easily seen by plotting the remeshed coordinates and coloring them based on their η-value (Figures 3.23a and 3.23c). The ξ values in the remeshed vessels are shown in Figures 3.23b and 3.23d.

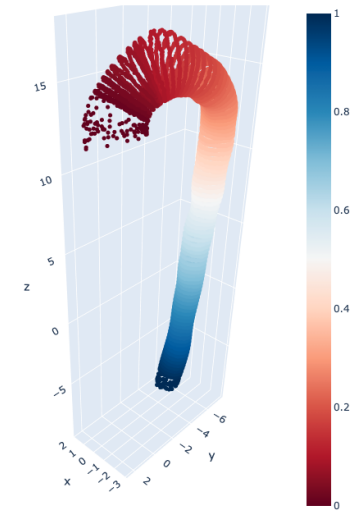

(a) 0063_1001 (η)

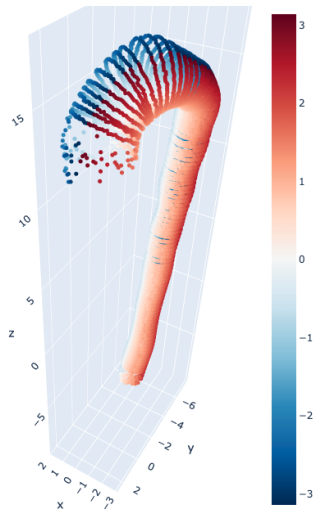

(b) 0063_1001 (ξ)

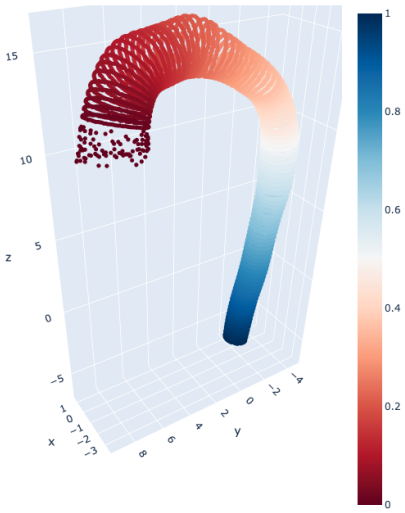

(c) 0075_1001 (η)

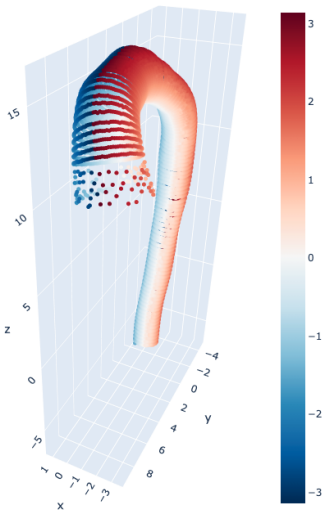

(d) 0075_1001 (ξ)

Figure 3.23: Scatter plot of remeshed vertices in the physical space colored according to their η- and ξ-values

One unintended result of the remeshing procedure was that the remeshed vertices

at the proximal and distal ends of the vessels were scattered and did not form ring-like structures (Figure 3.24). As mentioned previously, each ring in the physical domain corresponds to a level-set of η in the parametric domain; however, at the proximal and distal ends, the level-set did not form a discernible shape. This mostly likely occurred as a result of the parameterization scheme used in Chapter 3.3.

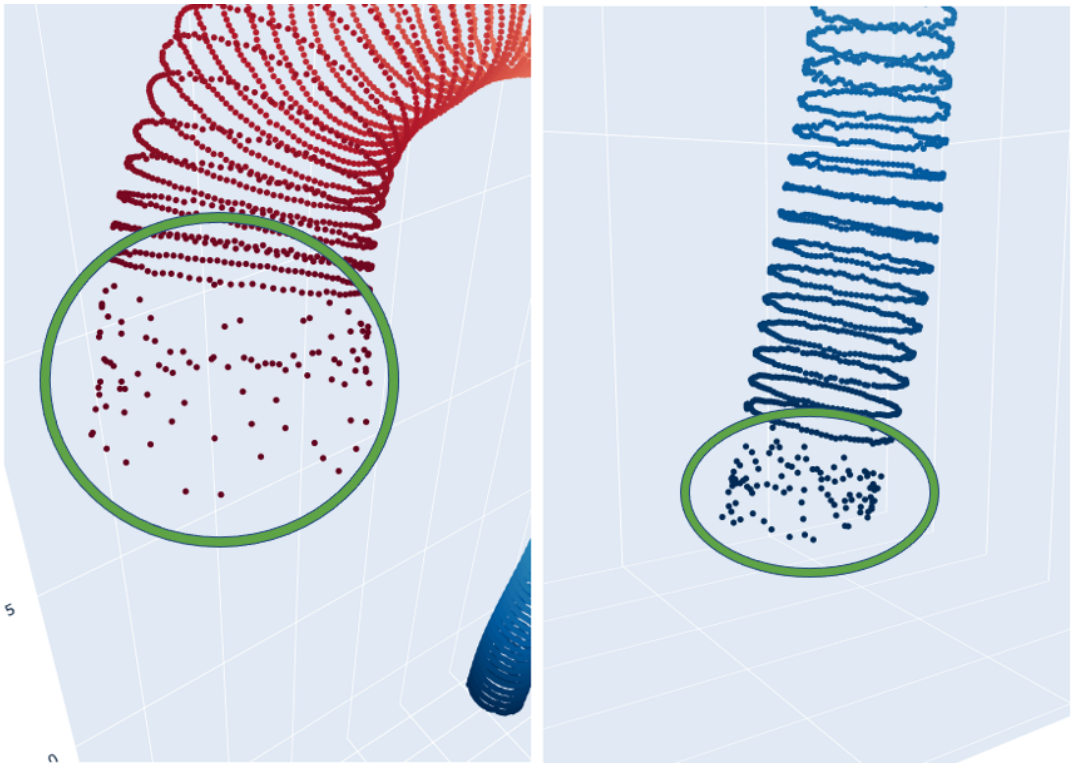

(a) Proximal end of 0075_1001 (b) Distal end of 0063_1001

Figure 3.24: Artifacts in remeshed vertices

3.8 Alignment

GPA was used to translate and rotate (scaling was set to one to maintain the size previously determined by centerline-based scaling in 3.5) the remeshed meshes such that they were all aligned to a common coordinate system. The steps for GPA are as follows:

1. Translate each mesh such that the centroid of each mesh is located at the origin
2. Randomly initialize one of the meshes to be the reference shape
3. For each of the meshes, calculate the rotation matrix that most closely maps it to the reference shape
4. Rotate each shape by its corresponding rotation matrix
5. Calculate the mean shape of the rotated shapes
6. Calculate the Procrustes distance between the mean shape and the reference shape
7. Set the new reference shape to be the mean shape
8. Repeat Steps 3 to 6 until the Procrustes distance is below a set threshold

The algorithm was used to align the scaled vessels with a threshold of 1×10^{-5} for Step 8. The rotation matrix for Step 3 was calculated using the `linalg.orthogonal_procrustes` function from SciPy [33, 45].

3.9 Principal Component Analysis

Once remeshed and aligned, each vessel was defined by the same number of points. Thus the remeshed values for x, y, z, and their corresponding GSDF values were used to define a matrix $X \in \mathbb{R}^{K \times 4N}$

$$X = \begin{bmatrix} x_1^{(1)} & y_1^{(1)} & z_1^{(1)} & G_1^{(1)} & \cdots & x_N^{(1)} & y_N^{(1)} & z_N^{(1)} & G_N^{(1)} \\ & \vdots & & & & & \vdots & & \\ x_1^{(k)} & y_1^{(k)} & z_1^{(k)} & G_1^{(k)} & \cdots & x_N^{(k)} & y_N^{(k)} & z_N^{(k)} & G_N^{(k)} \\ & \vdots & & & & & \vdots & & \\ x_1^{(K)} & y_1^{(K)} & z_1^{(K)} & G_1^{(K)} & \cdots & x_N^{(K)} & y_N^{(K)} & z_N^{(K)} & G_N^{(K)} \end{bmatrix} \tag{3.6}$$

where K is the number of vessels, N is the number of points per mesh, $x_i^{(j)}$ is the x-coordinate for the i-th point of the j-th remeshed mesh and similarly for $y_i^{(j)}$ and $z_i^{(j)}$, and $G_i^{(j)}$ is the GSDF for $\boldsymbol{x}_i^{(j)} = [x_i^{(j)}, y_i^{(j)}, z_i^{(j)}]$. It is similar to the matrix introduced in Equation 2.6 but with the addition of the GSDF for each vertex. The PCs of X were calculated using the sklearn implementation of PCA [46]. A visual representation of PCA on TAAs is shown in Figure 3.25[4].

[4]This representative figure uses the convention where each column represents a sample, as opposed to each row as in Equation 3.6, as it allowed for a better visualization of PCA

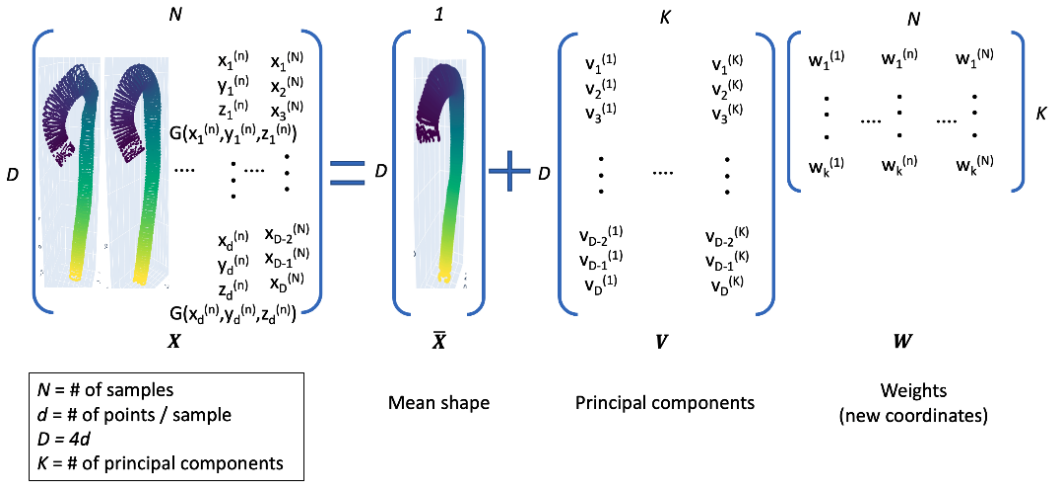

Figure 3.25: Visualization of PCA for TAAs with the GSDF

Though a maximum of 24 PCs could be returned, only the first ten PCs were kept for the following analyses as they captured more than 99% of the variance (Figure 3.26). As shown in the cumulative explained variance ratio plot in Figure 3.26, the first three PCs alone explained over 90% of the variation with the first, second, and third PCs accounting for 70%, 15%, and 7% of the variance, respectively.

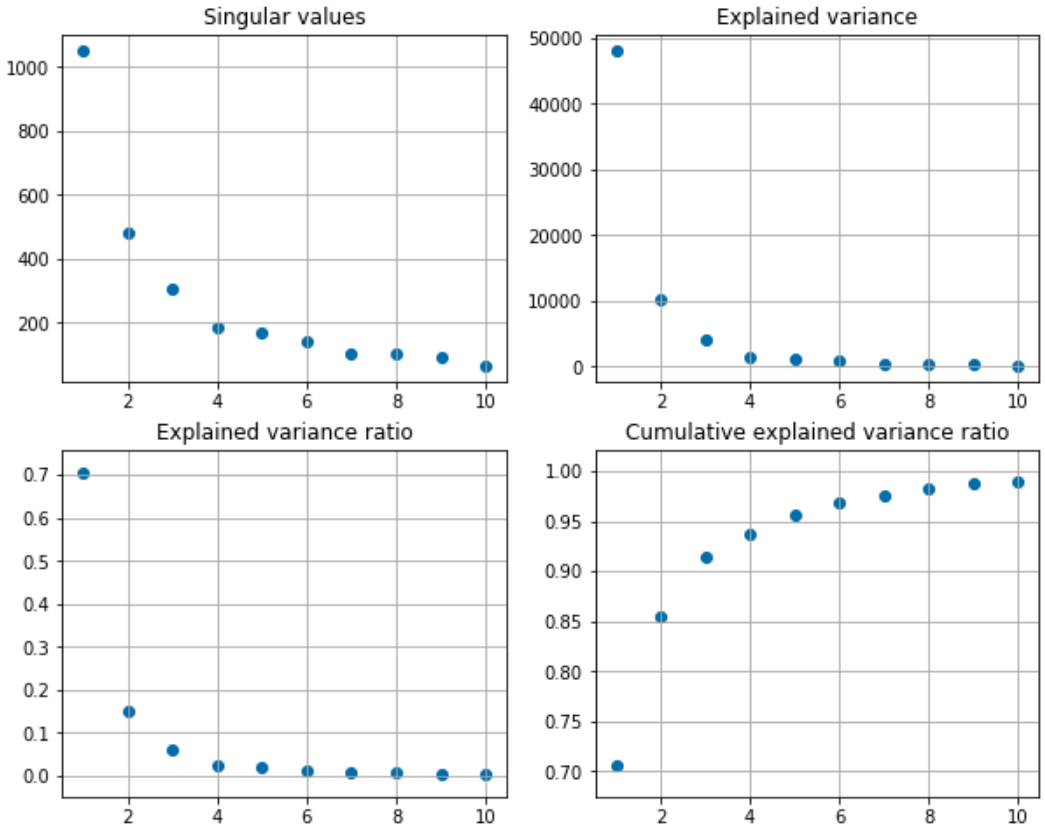

Figure 3.26: Variance, explained variance, explained variance ratio, and cumulative explained variance ratio as a function of the first ten principal components.

As a result of PCA, each of the shapes can be represented as the mean shape $\bar{X}$ added to a linear combination of the PCs V_i (Equation 3.7).

$$X^{(k)} \approx \bar{X} + \sum_{i=1}^{m} c_i^{(k)} \sqrt{\lambda_i} V_i \tag{3.7}$$

where $c_i^{(k)}$ represents the number of standard deviations away from the mean shape the k-th vessel is in the variation captured by the PC V_i.

3.9.1 Interpretation of principal components

The PCs can be better understood by observing the morphological variations captured by them. The changes in the shape of the vessel due to the first two PCs individually are shown in Figures 3.27 and Figure 3.28 where the middle vessel of both figures represents the mean shape. The horizontal axis represents the value of c_i in Equation 3.7.

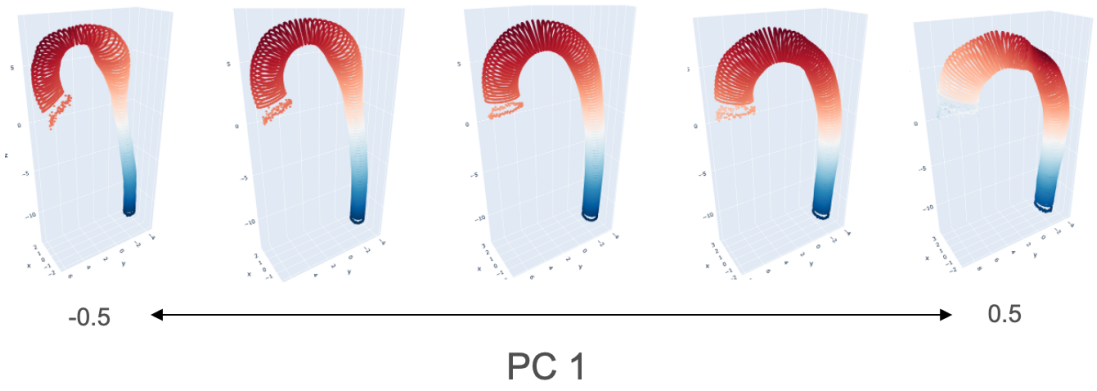

Figure 3.27: Morphological variation captured by PC 1 ($c_1 = [-0.5, -0.25, 0, 0.25, 0.5]$)

The first PC appears to modify the diameter of the distal end of the aortic arch or proximal end of the descending aorta. Increasing the value of c_1 causes the region to constrict, while decreasing the value leads to inflation. Furthermore, an increase in the value shifts the zero level-set of the GSDF distally and vice versa.

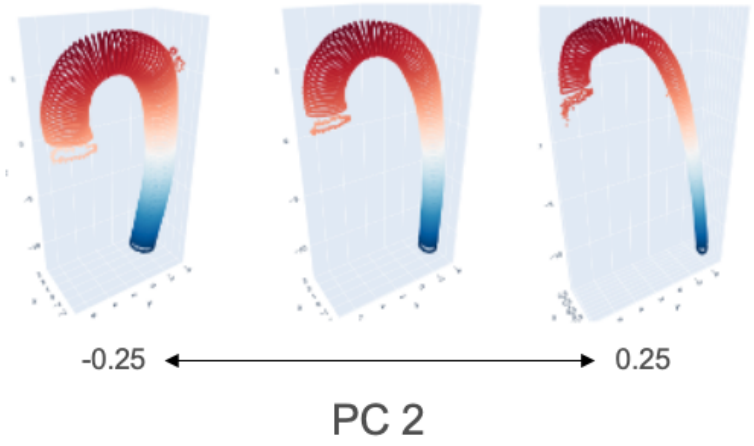

Figure 3.28: Morphological variation captured by PC 2 ($c_2 = [-0.25, 0, 0.25]$)

The variation captured by the second PC is limited to the geometry of the vessel as there seems to be very little variation in the location of the GSDF zero level-set. While the centerline of the vessel does not change, increasing c_2 decreases the overall diameter of the aorta and decreasing c_2 increases the diameter. The range of c_2 was limited as the geometry beyond the used range produced extreme geometries. The morphological variations captured by a combination of these two PCs is shown in Figure 3.29.

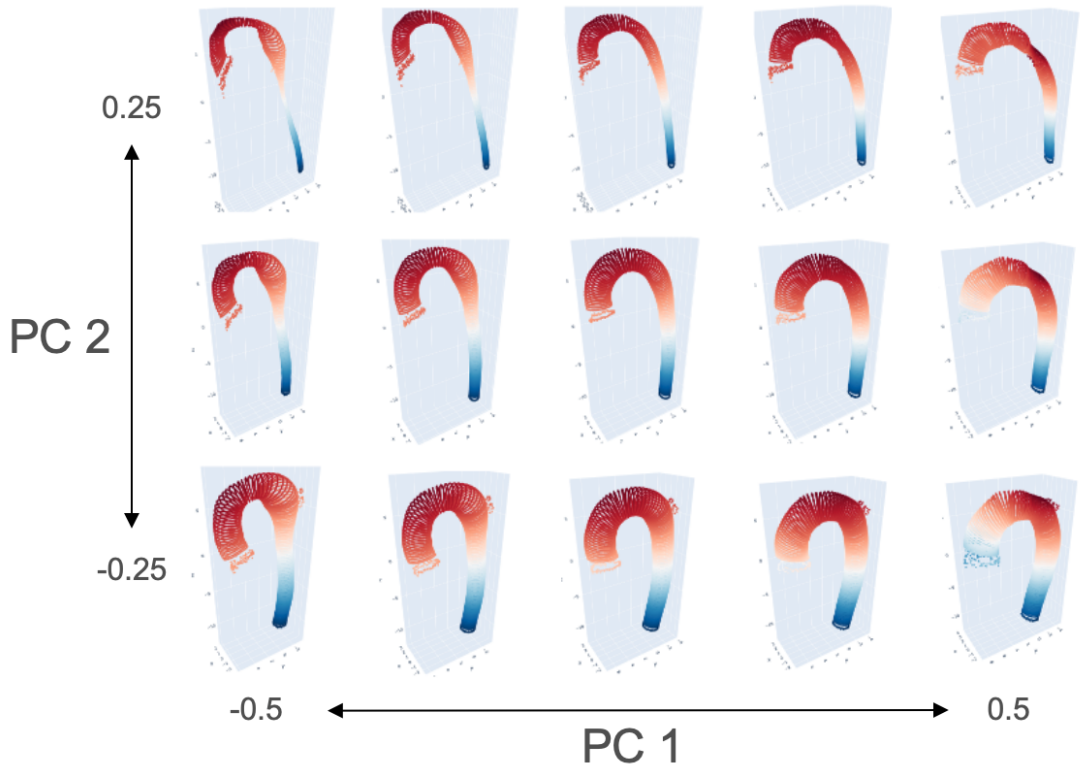

Figure 3.29: Morphological variations captured by first two PCs combined

Given that the first three PCs account for over 90% of the variation, the morphological characteristics of the third PC were observed as well (Figure 3.30).

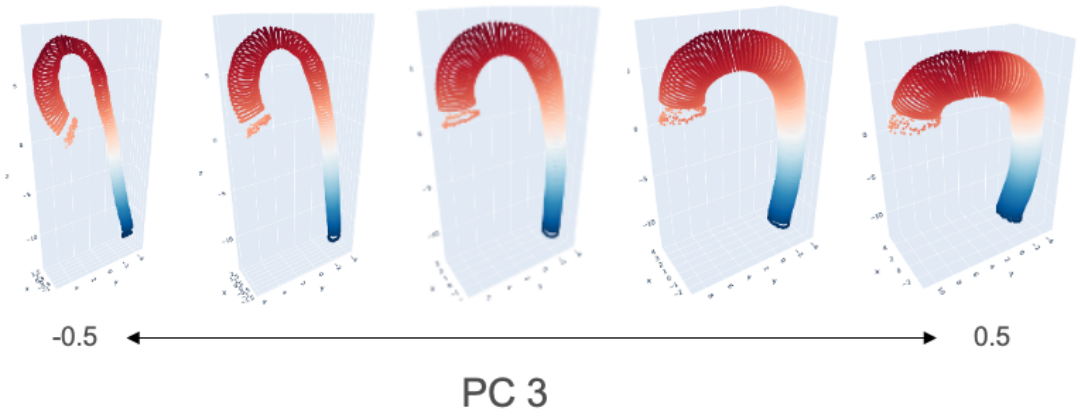

Figure 3.30: Morphological variation captured by PC 3 ($c_3 = [-0.5, -0.25, 0, 0.25, 0.5]$)

Though it may be challenging to recognize, the third PC accounted for the tortuosity of the vessel. This is better seen in an alternate view of the generated shapes with $c_3 = [-0.5, 0.5]$ (Figure 3.31). Here, the tortuosity is evident as a negative c_3 value leads to an increasingly tortuous and flattened vessel, whereas a positive c_3 leads to a similarly flattened vessel without the tortuosity.

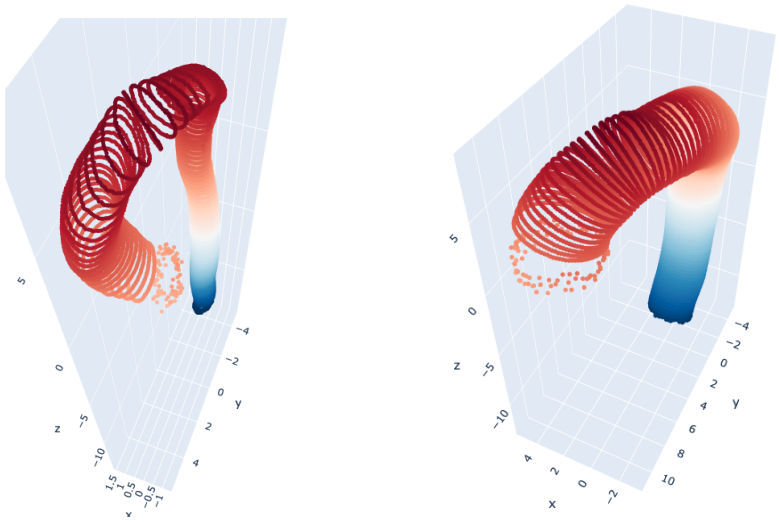

(a) $c_3 = -0.5$ (b) $c_3 = 0.5$

Figure 3.31: Alternate view of morphological variations captured by PC 3

3.10 Sample Reconstruction

As mentioned previously, each of the original vessels $X^{(k)}$ can be approximately reconstructed using Equation 3.7. The total variation captured by the PCs increases as m increases; therefore a larger m results in a more accurate reconstruction. Figure 3.32 demonstrates this through showing the reconstruction of one of the original vessels with varying numbers of PCs.

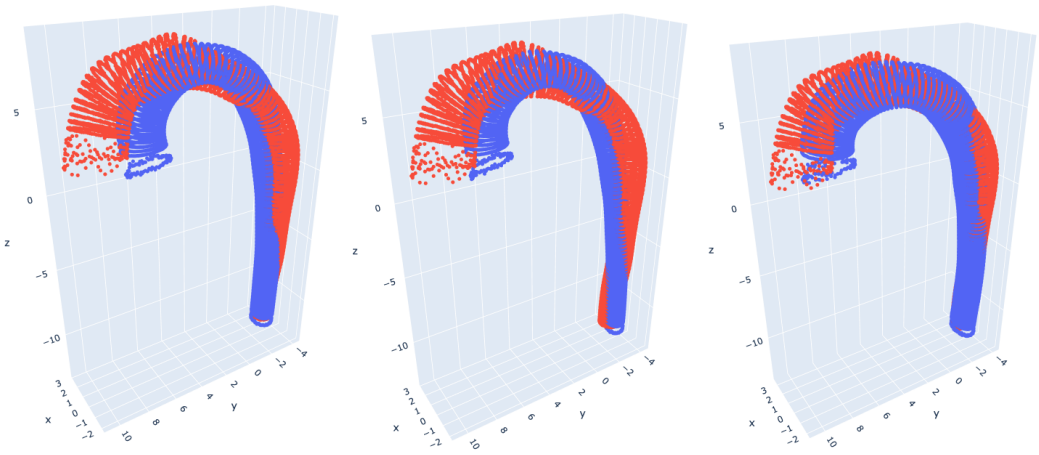

(a) $n = 1$ (b) $n = 2$ (c) $n = 3$

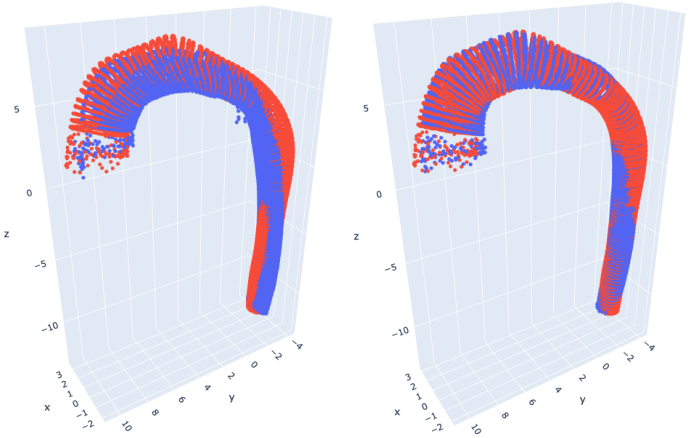

(d) $n = 5$ (e) $n = 8$

Figure 3.32: Approximate reconstruction (blue) of the original shape (red) of 0075_1001 using first n PCs

As expected, increasing the number of PCs used in the reconstruction yielded more accurate reconstructions of the original shapes. With 8 PCs, the vessel's geometry was reconstructed with negligible error.

A similar comparison was performed for the reconstruction of the original geometry and GSDF values. An accurate reconstruction of the GSDF required more PCs as shown in Figure 3.33. The figure shows the reconstructed vertices colored with their corresponding GSDF values where vertices with GSDF values less than zero are not plotted. Note that vertices on or very close to the boundary are colored in red. For the specific vessel shown below, the head vessel boundaries were clearly defined with 10 PCs (Figure 3.33e).

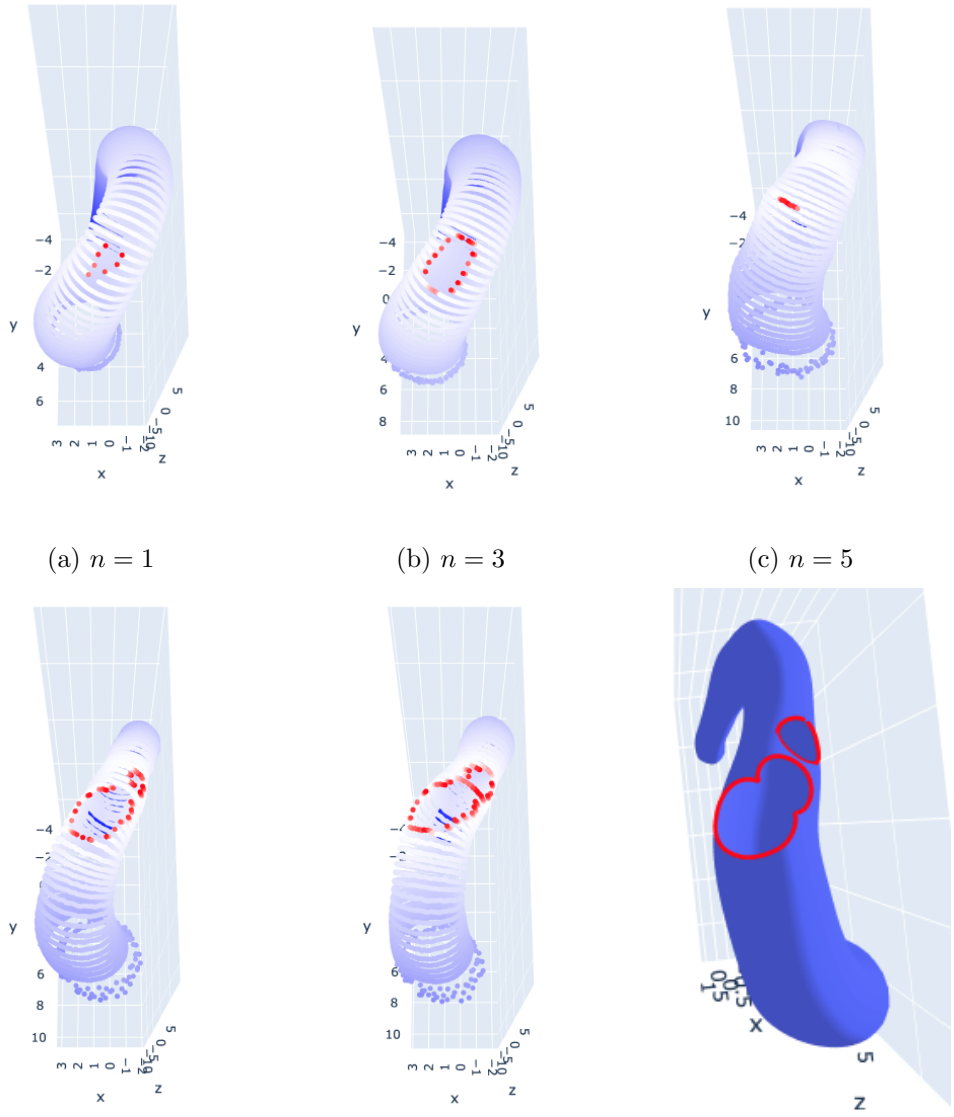

(a) $n = 1$ (b) $n = 3$ (c) $n = 5$

(d) $n = 8$ (e) $n = 10$ (f) Original

Figure 3.33: Reconstruction of the shape and GSDF of 0075_1001 using first n PCs

Using Equation 3.7, each of the vessels can be represented compactly by defining the PCs as a new basis for the "space of vessels". The coefficients $c_i\sqrt{\lambda_i}$ for the first

10 PCs for each sample is shown in a heatmap (Figure 3.34). The magnitude of the coefficients vary widely across the PCs due to the $\sqrt{\lambda_i}$ term. This is shown in the plot of the singular values in Figure 3.26 where the singular values decrease exponentially.

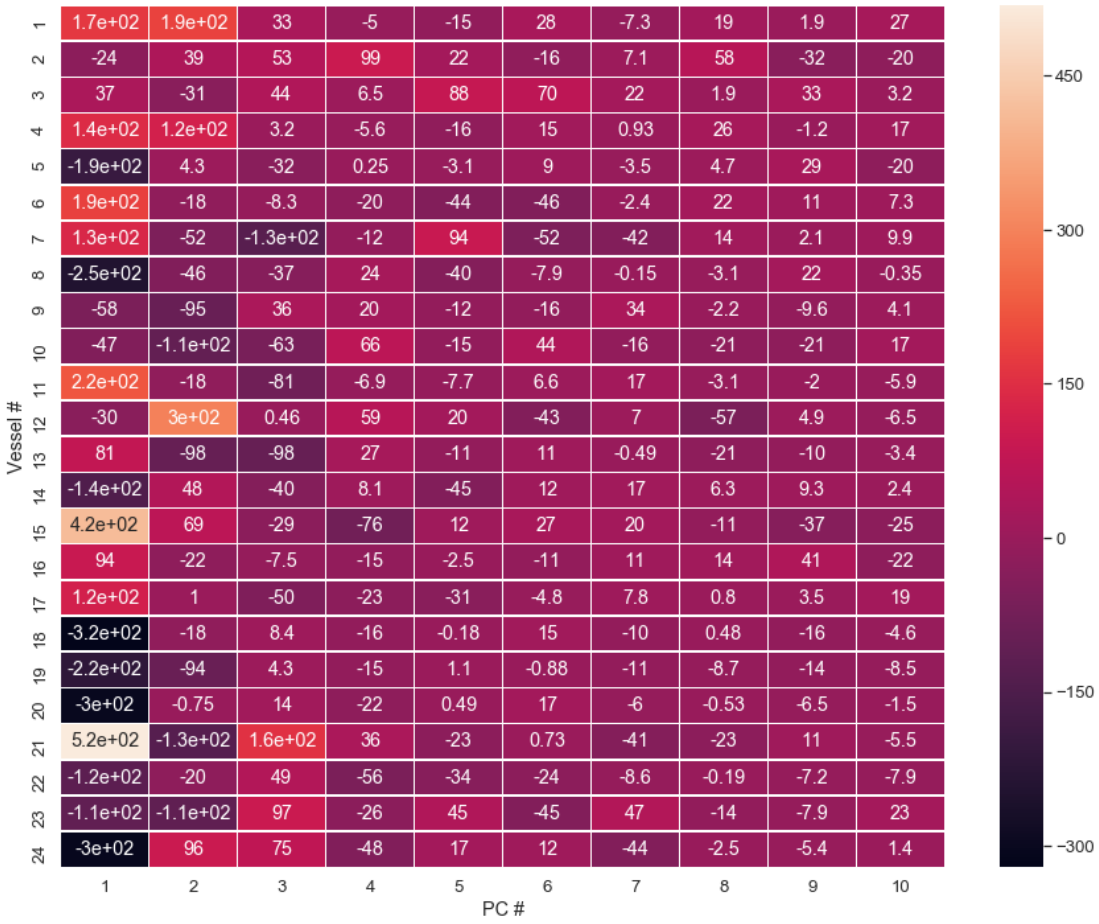

Figure 3.34: Heatmap of PC coefficients ($c_i\sqrt{\lambda_i}$) for sample reconstruction

By dividing each coefficient $c_i\sqrt{\lambda_i}$ by its corresponding singular value $\sqrt{\lambda_i}$, the PC coefficients can be normalized (Figure 3.35). These normalized coefficients c_i can be interpreted as the number of standard deviations away from the mean shape for a

particular PC.

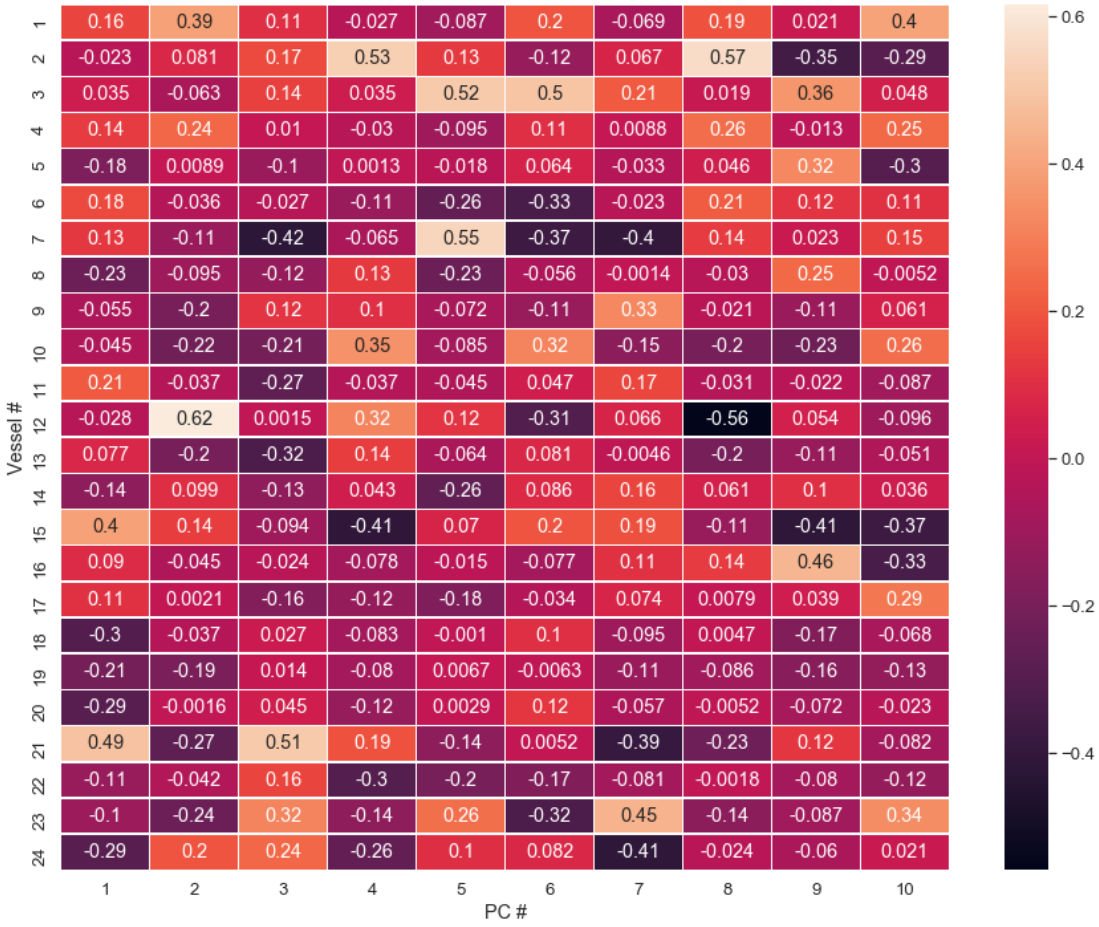

Figure 3.35: Heatmap of normalized PC coefficients (c_i) for sample reconstruction

Chapter 4

Discussion

In its current form, the proposed SSM framework has several limitations. First, an SSM will only account for variations observed in the original data, and therefore the SSM constructed in this thesis can only distinguish within pathological cases. In order to adequately evaluate TAAs, the data set used to construct the SSM will need to include non-pathological cases as well. Once a robust SSM is constructed, it can be paired with computational studies of the fluid and solid mechanics to identify geometric features, or biomarkers, prevalent in certain aortic pathologies that may be helpful in the clinical assessment of TAAs. A major challenge with these studies will be the determination of the various simulation parameters, especially the BCs. Since artificially synthesized geometries will have no physiologic measurements associated with them, a method for calculating these parameters is essential as they are known to cause large variations in the results.

Another limitation of the PCA-based SSM framework is the inability to uncover complex, nonlinear relationships in the data. Though other forms of matrix decomposition may be able to handle nonlinearities, they may do so at the loss of interpretability. PCA assumes that the original data can be approximately reconstructed as linear combinations of the PCs; therefore there exists a unique set of coefficients that best reconstructs each of the samples – the orthogonal projection of the sample onto the hyperplane defined by the span of the PCs. However, so long as the parameterization step exists, the full geometry of the branching vessels cannot be incorporated into the matrix decomposition-based SSM framework. Within the field of computer vision, researchers focused on shape representation learning have developed neural networks capable of handling complex geometries; however, these models require massive datasets to prevent overfitting – a luxury that may not be available in datasets of aortic geometry.

Instead of increasing the complexity of the models, additional features such as tissue thickness and material properties may be added into the SSM framework to further elucidate relationships between measurable characteristics of the aorta and clinically significant metrics. And although this thesis explores the possibility of augmenting the current SSM framework to better understand variations in morphology across individuals, the same framework could be used for longitudinal studies in healthy and pathological cases as well. Given the uncertainty associated not only with if an aneurysm will rupture or dissect, but also when an aneurysm will rupture or dissect, such studies may provide valuable insight into the medium- and long-term prognoses of patients known

to have TAAs.

As mentioned previously, given a sufficiently large sample size, increasingly complex models could be trained in place of the PCA-based SSM. Nevertheless, promising advances in machine learning (namely in federated learning and transfer learning) may lead to a paradigm shift in the processing of medical data. Shape representation learning within the field of computer vision has made substantial progress in the way complex geometries can be represented, and the adoption and adaptation of such techniques into the biomedical field will undoubtedly offer unique insights into the underlying pathophysiology of TAAs as well as other pathologies with a significant morphological component.

Bibliography

[1] OpenStax College, "Anatomy and Physiology."

[2] M. Piccinelli, "Parent Vessel Reconstruction."

[3] O. Nilsson, *Level-Set Methods and Geodesic Distance Functions*. PhD thesis, Linköping University, 2009.

[4] A. Harky, K. S. Fan, and K. H. Fan, "The genetics and biomechanics of thoracic aortic diseases," *Vascular Biology*, vol. 1, no. 1, pp. R13–R25, 2019.

[5] J. A. Elefteriades, A. Sang, G. Kuzmik, and M. Hornick, "Guilt by association: paradigm for detecting a silent killer (thoracic aortic aneurysm)," *Open Heart*, vol. 2, no. 1, p. e000169, 2015.

[6] T. K. M. Wang and M. Y. Desai, "Thoracic aortic aneurysm: Optimal surveillance and treatment," *Cleveland Clinic journal of medicine*, vol. 87, no. 9, pp. 557–568, 2020.

[7] L. A. Pape, T. T. Tsai, E. M. Isselbacher, J. K. Oh, P. T. O'Gara, A. Evangelista, R. Fattori, G. Meinhardt, S. Trimarchi, E. Bossone, T. Suzuki, J. V. Cooper, J. B. Froehlich, C. A. Nienaber, and K. A. Eagle, "Aortic diameter 5.5 cm is not a good predictor of type A aortic dissection: Observations from the International Registry of Acute Aortic Dissection (IRAD)," *Circulation*, vol. 116, no. 10, pp. 1120–1127, 2007.

[8] J. Wu, M. A. Zafar, Y. Li, A. Saeyeldin, Y. Huang, R. Zhao, J. Qiu, M. Tanweer, M. Abdelbaky, A. Gryaznov, J. Buntin, B. A. Ziganshin, S. K. Mukherjee, J. A. Rizzo, C. Yu, and J. A. Elefteriades, "Ascending Aortic Length and Risk of Aortic Adverse Events: The Neglected Dimension," *Journal of the American College of Cardiology*, vol. 74, no. 15, pp. 1883–1894, 2019.

[9] L. N. Girardi, C. Lau, and I. Gambardella, "Aortic dimensions as predictors of adverse events," *Journal of Thoracic and Cardiovascular Surgery*, vol. 161, no. 4, pp. 1193–1197, 2021.

[10] Centers for Disease Control and Prevention, "Aortic Aneurysm," 2020.

[11] V. L. Gott, P. S. Greene, D. E. Alejo, D. E. Cameron, D. C. Naftel, C. Miller, A. M. Gillinov, J. C. Laschinger, and R. E. Pyeritz, "Replacement of the aortic root in patients with Marfan's syndrome," *The New England Journal of Medicine*, vol. 340, no. 17, pp. 1307–1313, 1999.

[12] A. L. Marsden, "Optimization in cardiovascular modeling," *Annual Review of Fluid Mechanics*, vol. 46, pp. 519–546, 2014.

[13] M. Owais Khan, V. T. Arana, C. Rubbert, J. F. Cornelius, I. Fischer, R. Bostelmann, H. J. Mijderwijk, B. Turowski, H. J. Steiger, R. May, and A. K. Petridis, "Association between aneurysm hemodynamics and wall enhancement on 3D vessel wall MRI," *Journal of Neurosurgery*, vol. 134, no. 2, pp. 565–575, 2021.

[14] F. Joly, G. Soulez, S. Lessard, C. Kauffmann, and I. Vignon-Clementel, "A Cohort Longitudinal Study Identifies Morphology and Hemodynamics Predictors of Abdominal Aortic Aneurysm Growth," *Annals of Biomedical Engineering*, vol. 48, no. 2, pp. 606–623, 2020.

[15] M. Shojima, "Magnitude and Role of Wall Shear Stress on Cerebral Aneurysm. Computational Fluid Dynamic Study of 20 Middle Cerebral Artery Aneurysms," *Stroke*, pp. 2500–2505, 2004.

[16] P. Youssefi, A. Gomez, T. He, L. Anderson, N. Bunce, R. Sharma, C. A. Figueroa, and M. Jahangiri, "Patient-specific computational fluid dynamics—assessment of aortic hemodynamics in a spectrum of aortic valve pathologies," *Journal of Thoracic and Cardiovascular Surgery*, vol. 153, no. 1, pp. 8–20, 2017.

[17] R. Jayendiran, F. Condemi, S. Campisi, M. Viallon, P. Croisille, and S. Avril,

"Computational prediction of hemodynamical and biomechanical alterations induced by aneurysm dilatation in patient-specific ascending thoracic aortas," *International Journal for Numerical Methods in Biomedical Engineering*, vol. 36, no. 6, pp. 1–24, 2020.

[18] K. D. Dennis, D. F. Kallmes, and D. Dragomir-Daescu, "Cerebral aneurysm blood flow simulations are sensitive to basic solver settings," *Journal of Biomechanics*, vol. 57, pp. 46–53, 2017.

[19] D. A. Steinman, Y. Hoi, P. Fahy, L. Morris, M. T. Walsh, N. Aristokleous, A. S. Anayiotos, Y. Papaharilaou, A. Arzani, S. C. Shadden, P. Berg, G. Janiga, J. Bols, P. Segers, N. W. Bressloff, M. Cibis, F. H. Gijsen, S. Cito, J. Pallarés, L. D. Browne, J. A. Costelloe, A. G. Lynch, J. Degroote, J. Vierendeels, W. Fu, A. Qiao, S. Hodis, D. F. Kallmes, H. Kalsi, Q. Long, V. O. Kheyfets, E. A. Finol, K. Kono, A. M. Malek, A. Lauric, P. G. Menon, K. Pekkan, M. Esmaily Moghadam, A. L. Marsden, M. Oshima, K. Katagiri, V. Peiffer, Y. Mohamied, S. J. Sherwin, J. Schaller, L. Goubergrits, G. Usera, M. Mendina, K. Valen-Sendstad, D. F. Habets, J. Xiang, H. Meng, Y. Yu, G. E. Karniadakis, N. Shaffer, and F. Loth, "Variability of computational fluid dynamics solutions for pressure and flow in a giant aneurysm: The ASME 2012 summer bioengineering conference CFD challenge," *Journal of Biomechanical Engineering*, vol. 135, no. 2, 2013.

[20] K. Valen-Sendstad, A. W. Bergersen, Y. Shimogonya, L. Goubergrits, J. Bruening,

J. Pallares, S. Cito, S. Piskin, K. Pekkan, A. J. Geers, I. Larrabide, S. Rapaka, V. Mihalef, W. Fu, A. Qiao, K. Jain, S. Roller, K. A. Mardal, R. Kamakoti, T. Spirka, N. Ashton, A. Revell, N. Aristokleous, J. G. Houston, M. Tsuji, F. Ishida, P. G. Menon, L. D. Browne, S. Broderick, M. Shojima, S. Koizumi, M. Barbour, A. Aliseda, H. G. Morales, T. Lefèvre, S. Hodis, Y. M. Al-Smadi, J. S. Tran, A. L. Marsden, S. Vaippummadhom, G. A. Einstein, A. G. Brown, K. Debus, K. Niizuma, S. Rashad, S. i. Sugiyama, M. Owais Khan, A. R. Updegrove, S. C. Shadden, B. M. Cornelissen, C. B. Majoie, P. Berg, S. Saalfield, K. Kono, and D. A. Steinman, "Real-World Variability in the Prediction of Intracranial Aneurysm Wall Shear Stress: The 2015 International Aneurysm CFD Challenge," *Cardiovascular Engineering and Technology*, vol. 9, no. 4, pp. 544–564, 2018.

[21] A. Updegrove, N. M. Wilson, J. Merkow, H. Lan, A. L. Marsden, and S. C. Shadden, "SimVascular: An Open Source Pipeline for Cardiovascular Simulation," *Annals of Biomedical Engineering*, vol. 45, no. 3, pp. 525–541, 2017.

[22] F. Ambellan, H. Lamecker, C. von Tycowicz, and S. Zachow, "Biomedical Visualisation," in *Advances in Experimental Medicine and Biology*, ch. Statistica, pp. 67–84, Springer, Cham, 2019.

[23] W. Keustermans, T. Huysmans, F. Danckaers, A. Zarowski, B. Schmelzer, J. Sijbers, and J. J. Dirckx, "High quality statistical shape modelling of the human nasal cavity and applications," *Royal Society Open Science*, vol. 5, no. 12, 2018.

[24] R. J. Barr, J. S. Gregory, K. Yoshida, S. Alesci, R. M. Aspden, and D. M. Reid, "Significant morphological change in osteoarthritic hips identified over 6–12 months using statistical shape modelling," *Osteoarthritis and Cartilage*, vol. 26, no. 6, pp. 783–789, 2018.

[25] A. C. Vrancken, S. P. Crijns, M. J. Ploegmakers, C. O'Kane, T. G. van Tienen, D. Janssen, P. Buma, and N. Verdonschot, "3D geometry analysis of the medial meniscus - A statistical shape modeling approach," *Journal of Anatomy*, vol. 225, no. 4, pp. 395–402, 2014.

[26] N. Rodriguez-Florez, J. L. Bruse, A. Borghi, H. Vercruysse, J. Ong, G. James, X. Pennec, D. J. Dunaway, N. U. Jeelani, and S. Schievano, "Statistical shape modelling to aid surgical planning: associations between surgical parameters and head shapes following spring-assisted cranioplasty," *International Journal of Computer Assisted Radiology and Surgery*, vol. 12, no. 10, pp. 1739–1749, 2017.

[27] J. L. Bruse, K. McLeod, G. Biglino, H. N. Ntsinjana, C. Capelli, T. Y. Hsia, M. Sermesant, X. Pennec, A. M. Taylor, S. Schievano, A. Taylor, A. Giardini, S. Khambadkone, M. de Leval, E. Bove, A. Dorfman, G. H. Baker, A. Hlavacek, F. Migliavacca, G. Pennati, G. Dubini, A. Marsden, I. Vignon-Clementel, R. Figliola, and J. McGregor, "A statistical shape modelling framework to extract 3D shape biomarkers from medical imaging data: Assessing arch morphology of repaired coarctation of the aorta," *BMC Medical Imaging*, vol. 16, no. 1, pp. 1–19,

2016.

[28] J. L. Bruse, M. A. Zuluaga, A. Khushnood, K. McLeod, H. N. Ntsinjana, T. Y. Hsia, M. Sermesant, X. Pennec, A. M. Taylor, and S. Schievano, "Detecting Clinically Meaningful Shape Clusters in Medical Image Data: Metrics Analysis for Hierarchical Clustering Applied to Healthy and Pathological Aortic Arches," *IEEE Transactions on Biomedical Engineering*, vol. 64, no. 10, pp. 2373–2383, 2017.

[29] L. Liang, M. Liu, C. Martin, J. A. Elefteriades, and W. Sun, "A machine learning approach to investigate the relationship between shape features and numerically predicted risk of ascending aortic aneurysm," *Biomechanics and Modeling in Mechanobiology*, vol. 16, no. 5, pp. 1519–1533, 2017.

[30] J. P. Schmidt, S. L. Delp, M. A. Sherman, C. A. Taylor, V. S. Pande, and R. B. Atlamn, "The Simbios National Cencter: Systems Biology in Motion," *Proc IEEE Inst Electr Electron Eng*, vol. 96, no. 8, pp. 1226–1280, 2008.

[31] R. Izzo, D. Steinman, S. Manini, and L. Antiga, "The Vascular Modeling Toolkit: A Python Library for the Analysis of Tubular Structures in Medical Images," *Journal of Open Source Software*, vol. 3, no. 25, p. 745, 2018.

[32] C. Goodall, "Procrustes Methods in the Statistical Analysis of Shape," *Journal of the Royal Statistical Society. Series B (Methodological)*, vol. 53, no. 2, pp. 285–339, 1991.

[33] P. H. Schönemann, "A generalized solution of the orthogonal procrustes problem," 1966.

[34] K. Pearson, "On lines and planes of closest fit to systems of points in space," *The London, Edinburgh, and Dublin Philosophical Magazine and Journal of Science*, vol. 2, no. 11, pp. 559–572, 1901.

[35] G. Van Rossum and F. L. Drake, *Python 3 Reference Manual*. Scotts Valley, CA: CreateSpace, 2009.

[36] T. Kluyver, B. Ragan-Kelley, F. Pérez, B. Granger, M. Bussonnier, J. Frederic, K. Kelley, J. Hamrick, J. Grout, S. Corlay, P. Ivanov, D. Avila, S. Abdalla, and C. Willing, "Jupyter Notebooks—a publishing format for reproducible computational workflows," in *Positioning and Power in Academic Publishing: Players, Agents and Agendas - Proceedings of the 20th International Conference on Electronic Publishing, ELPUB 2016*, pp. 87–90, 2016.

[37] P. T. Inc., "Collaborative data science," 2015.

[38] J. D. Hunter, "Matplotlib: A 2D Graphics Environment," *Computing in Science & Engineering*, vol. 9, no. 3, pp. 90–95, 2007.

[39] B. D. Team, "Bokeh: Python library for interactive visualization."

[40] W. Schroeder, K. Martin, and B. Lorensen, *The Visualization Toolkit*. Kitware, 4 ed., 2006.

[41] Autodesk, "Meshmixer," 2018.

[42] M. Piccinelli, "Mapping and Patching."

[43] J. S. Gao, A. G. Huth, M. D. Lescroart, and J. L. Gallant, "Pycortex: An interactive surface visualizer for fMRI," *Frontiers in Neuroinformatics*, vol. 9, no. September, pp. 1–12, 2015.

[44] J. D. Hunter, "Matplotlib: A 2D Graphics Environment," *Computing in Science & Engineering*, vol. 9, no. 3, pp. 90–95, 2007.

[45] P. Virtanen, R. Gommers, T. E. Oliphant, M. Haberland, T. Reddy, D. Cournapeau, E. Burovski, P. Peterson, W. Weckesser, J. Bright, S. J. van der Walt, M. Brett, J. Wilson, K. J. Millman, N. Mayorov, A. R. J. Nelson, E. Jones, R. Kern, E. Larson, C. J. Carey, İ. Polat, Y. Feng, E. W. Moore, V. Jake, D. Laxalde, J. Perktold, R. Cimrman, I. Henriksen, E. A. Quintero, C. R. Harris, A. M. Archibald, A. H. Ribeiro, F. Pedregosa, P. van Mulbregt, and S. . Contributors, "SciPy 1.0: Fundamental Algorithms for Scientific Computing in Python," *Nature Methods*, vol. 17, no. 3, pp. 261–272, 2020.

[46] F. Pedregosa, G. Varoquaux, A. Gramfot, V. Michel., B. Thirion, O. Grisel, M. Blondel, P. Prettenhofer, R. Weiss, V. Dubourg, J. Vanderplas, A. Passos, D. Cournapeau, M. Brucher, M. Perrot, and E. Duchesnay, "Scikit-learn: Machine Learning in Python," *Journal of Machine Learning Research*, vol. 12, no. 85, pp. 2825–2830, 2011.